The Effect of Grid Resolution on Hydrodynamic Modeling of Biscayne Bay

by

Nathaniel Azubuike Nwogwu

A thesis submitted to the Graduate Faculty of
Auburn University
in partial fulfillment of the
requirements for the Degree of
Master of Science in Biosystems Engineering

Auburn, Alabama
December 10, 2023

Keywords: Hydrodynamic modeling, EFDC+, Grid resolution, Water surface elevation, Estuaries, Salinity, Florida

Approved by

Anna C. Linhoss, Chair, Associate Professor, Department of Biosystems Engineering
Xing Fang, Committee member, Professor, Department of Civil and Environmental Engineering
Jasmeet Lamba, Committee member, Associate Professor, Department of Biosystems Engineering

Abstract

Environmental Fluid Dynamics Code Plus (EFDC+) is a model that has been proven to be effective in hydrodynamic simulation. Understanding water surface elevation (WSE) and salinity dynamics in estuaries is crucial for comprehending the complex interplay of these vital hydrodynamic parameters, as they significantly influence ecological processes, water quality, and habitat suitability in these critical coastal ecosystems. The study aims to develop and assess five EFDC+ models with varying resolutions for Biscayne Bay (BB), Florida. The impact of grid resolution on model performance in WSE and salinity simulations was explored by comparing model outputs with observational data. The study employed a Medium-resolution model grid as a baseline, featuring a finer resolution (~130 m × 130 m) in North BB and a coarser resolution (~300 m × 300 m) in Central and South BB, seamlessly integrated. The Fine-resolution model was created by halving the "i-direction" and "j-direction" of the Medium-resolution grid; in contrast, the Coarse2-, Coarse3-, and Coarse4-resolution models are developed by multiplying these directions by factors of 2, 3, and 4, respectively. All models adopted the WGS 84 UTM zone 17N coordinate system, with meters as the unit of measurement. A geo-processed bathymetry at a 20 m x 20 m horizontal spatial resolution and 0.01 m vertical accuracy, along with other input data from Alarcon et al. (2022), was utilized for simulations spanning January 2012 to December 2018, with a warm-up phase from January 2017 to June 2017. The assessment of WSE simulation at three measurement stations consistently showed performance trends across models. The accuracy of model simulations exhibited a gradual reduction, ranging from -0.1 cm to 1.7 cm, with an increasing trend as resolution decreases. Salinity simulations, categorized into four regions, exhibit varying model performance. While models generally performed poorly and irregularly in salinity simulation and consistently fare better in simulating salinity in Open and South Bay sections, challenges arise in accurately replicating low salinity levels below 15 ppt in Nearshore locations. Notably, the North Bay division shows greater variability across resolutions, with Coarse3 and Coarse4 models diverging greatly from others. The results suggest a need for the establishment of salinity measurement stations at the tidal open mouths of the Bay or using HYbrid Coordinate Ocean Model (HYCOM) salinity data for the tidal BCs. Also, installing salinity measurement stations in the North Bay is essential. This initiative is crucial for conducting studies that can yield improved results and management recommendations, particularly given the intricate geometry and potential complexities in dynamics.

Acknowledgments

I would like to express my deepest gratitude to my advisor, Dr. Anna C. Linhoss, for her guidance, invaluable insights, and continuous support throughout my master's journey. Her mentorship has been instrumental in shaping my research and academic growth.

I extend my sincere appreciation to the National Oceanic and Atmospheric Administration for providing the funding that made this research possible. Their support has allowed me to delve into meaningful investigations and contribute to the body of knowledge in my field. I am truly thankful for the opportunities and resources this organization has generously provided.

I am indebted to my committee members, Professor Xing Fang, and Dr. Jasmeet Lamba, for their constructive feedback and scholarly contributions, which significantly enhanced the quality of my thesis. I also want to acknowledge the Department Head, Professor Oladiran Fasina, for his mentorship and encouragement. I also extend my appreciation to the dedicated staff of the Department of Biosystems Engineering, and my fellow lab members for their collaborative spirit, creating a conducive academic environment.

Lastly, my heartfelt thanks go to my mom, Patricia, my wife, Philomina, and my siblings: Jacinta, Lazarus, and Jacob. To my late dad, Simeon Onwe, who died during my first semester at Auburn University, I remain grateful for all your teachings and mentorship. My appreciation goes to my friends for their unwavering encouragement throughout this academic journey. Their emotional support has been my pillar of strength. To my mentors, Dr. F.O. Ajibade and Dr. C. Nzediegwu, who have shared their wisdom and experiences and encouraged me throughout the research process - thank you all for being an integral part of my master's experience.

Table of Contents

List of Tables

List of Figures

List of Abbreviations

2D	Two Dimensional
3D	Three Dimensional
SWEs	Shallow Water Equations
EFDC	Environmental Fluid Dynamics Computer Code
EFDC+	Environmental Fluid Dynamics Computer Code Plus
BB	Biscayne Bay
DHI	Danish Hydraulic Institute
GPUs	Graphical Processing Units
POM	Princeton Ocean Model
NCOM	Navy Coastal Ocean Model
FVCOM	Finite Volume Coastal Ocean Model
CPU	Central Processing Units
ELCOM	Estuary, Lake, and Coastal Ocean Model
LLC	Limited liability Company
DSI	Dynamic Solutions International
DEM	Digital Elevation Model
NOAA	National Oceanic and Atmospheric Administration
NCEI	National Centers for Environmental Information
UTM	Universal Transverse Mercator
NetCDF	Network Common Data Form
NAVD	North American Vertical Datum
SFWMD	South Florida Water Management District

WGS	World Geodetic System
BC	Boundary Condition
R^2	Coefficient of determination
RSR	RMSE-observations standard deviation ratio
KGE	Kling-Gupta efficiency
NSE	Nash-Sutcliffe Efficiency
HYCOM	HYbrid Coordinate Ocean Model

Chapter 1 Introduction

1.1 Background

Employing numerical modeling to simulate complex hydrodynamics yields valuable insights, elucidating circulation patterns, water levels, velocity, temperature fluctuations, and stratification processes. These insights are crucial in understanding how factors influence the transportation of pollutants and the overall water quality within a given water body (Cedillo, 2015). The application of numerical models becomes even more important for coastlines composed of complex shapes. These shapes result from different processes, such as erosion, sedimentation, hydrodynamics, anthropogenic influence, and tectonic activity. The complexity of these shapes can significantly influence the flow of both tidal and freshwater systems in the surrounding area.

1.2 Numerical Models

Numerical models are mathematical equations that find an approximate solution to a physical system or phenomenon. Numerical models can be used to represent physical systems, such as water flow in coastal areas; hence, they can be used to simulate and predict the behavior of the system. Numerical modeling is useful because of its effectiveness in approximating complex systems (e.g., most nonlinear systems) where mathematical problems are too difficult to solve using analytical solutions.

Numerical modeling generally involves interpolation, derivatives, integration, and root finding (nonlinear and differential equations). The kind of equation, linear, nonlinear, or differential (ordinary or partial) – determines which numerical approach is chosen. Numerical models can be constructed using the laws of physics, such as the conservation of mass and energy and mechanistic

principles. Physically based numerical models can be used to simulate the behavior of the system over time and space under different conditions.

1.3 Hydrodynamic Models

Hydrodynamic models are a specific type of physically based numerical model designed to simulate and predict the behavior of fluids, such as water and air. Hydrodynamic models use mathematical equations to describe the behavior of fluids, including the motion of fluid particles and the interactions between particles. The equations are solved using numerical methods, which allow the models to simulate complex fluid behavior, such as turbulence and wave propagation. Such equations are often based on the 2D Shallow Water Equations (SWEs) derived from the fundamental Navier-Stokes equations, which are rooted in mass (equation 1) and momentum (equations 2a and 2b) conservation principles (Hagen, 2014). Equation 3 denotes the Coriolis parameter, which quantifies the impact of the earth's rotation on the system, and equation 4 denotes the lateral stresses, encompassing factors such as viscous friction, turbulent friction, and differential advection. The Navier-Stokes equations are inherently complex; thus, some assumptions are made to simplify them. The Navier-Stokes equations operate under the assumption that the fluid is treated as a continuous medium rather than a collection of individual particles within the specific scale of concern. Another essential assumption is that all the relevant fields, such as pressure, flow velocity, density, and temperature, exhibit a certain degree of smooth differentiability (UC Davis Math, 2012). Also, the SWEs are predicated on the assumption that the vertical scale, H, is significantly smaller than the horizontal scale, L. This condition places the fluid flows in the category of boundary-layer type flows. (Vreugdenhil, 1994).

$$\frac{\delta}{\delta t} + \frac{\delta}{\delta x}(hu) + \frac{\delta}{\delta y}(hv) = 0 \quad \ldots\ldots (1)$$

$$\frac{\delta}{\delta t}(hu) + \frac{\delta}{\delta x}(hu^2) + \frac{\delta}{\delta y}(huv) - fhv + gh\frac{\delta \xi}{\delta x} + \frac{gh^2\delta\rho}{2\rho_0\delta x} - \frac{1}{\rho_0}\tau_{bx} - \frac{\delta}{\delta x}(hT_{xx}) - \frac{\delta}{\delta y}\left(hT_{xy}\right) = F_x$$

…… (2a)

$$\frac{\delta}{\delta t}(hv) + \frac{\delta}{\delta x}(huv) + \frac{\delta}{\delta y}(hv^2) - fhu + gh\frac{\delta \zeta}{\delta x} + \frac{gh^2\delta\rho}{2\rho_0\delta y} - \frac{1}{\rho_0}\tau_{by} - \frac{\delta}{\delta x}\left(hT_{xy}\right) - \frac{\delta}{\delta y}\left(hT_{yy}\right) = F_y$$

…… (2b)

$$f = 2\Omega sin\Phi$$ …… (3)

$$T_{ij} = \frac{1}{h}\int_0^h (v(\frac{\delta u_i}{\delta x_j} + \frac{\delta u_j}{\delta x_i}) - \overline{u_i' u_j'} + (u_i - \bar{u}_i)(u_j - \bar{u}_j))\, dz$$ …….... (4)

Where:

h represents the water depth.

u signifies the flow velocity in the x-direction

v represents the flow velocity in the y-direction

f stands for the Coriolis parameter, which accounts for the Earth's rotational effect.

g denotes gravitational acceleration.

ζ represents the water surface elevation measured above the vertical reference level in meters(m).

ρ signifies the fluid density.

τ_b corresponds to the bed shear stress, which measures friction on the bed.

T_{ij} encompasses the lateral stresses, which include components like viscous friction, turbulent friction, and differential advection.

F denotes the external driving forces, including factors like wind stress.

Ω represents the angular revolution rate of the Earth.

Φ stands for geographical latitude.

The 'ν' in equation 4 represents viscosity.

Hydrodynamic models are constantly being improved and updated as new data becomes available, making them valuable tools for understanding and managing the complex dynamics of fluid systems. Several hydrodynamic models have been used to simulate and predict fluid flow and transport phenomena in various applications, including oceanography, meteorology, engineering, and environmental science. A few examples of hydrodynamic models include the Princeton Ocean Model (Blumberg & Mellor, 1987), the Environmental Fluid Dynamics Computer Code (Hamrick, 1992), Storm Surge Model (Luettich et al., 1992), General Ocean Turbulence Model (Burchard et al., 1999), and Finite-Volume Coastal Ocean Model (Chen et al., 2003). These hydrodynamic models use grids as a fundamental component. Grids provide a way to discretize the continuous space and equations governing fluid motion into a numerical form that can be solved on a computer.

1.4 Computational Grid

A grid is a way to divide the spatial area of a numerical model into discrete areas or cells so that the model can make calculations within each cell. A grid is a collection of cells formed by connecting the pairs of discretization-defined vertices along edges. A cell is a building block that makes up a grid. A simple grid illustration is graph paper where you draw graphs. Grids can be two-dimensional or three-dimensional. The resolution of the grid is an essential aspect of the model, as it determines the level of detail that the model can simulate. The finer the grid, the more

detailed the simulation, but also the more computational resources are needed. In a hydrodynamic model, each cell represents a specific volume, the water within that cell, and various water properties such as depth, salinity, and temperature.

Structured and unstructured grids are the two main types of grids. As the name suggests, structured grids are those grids with a fundamental rectangular matrix that facilitates storage and use by allowing access to individual data points via integer offsets, which are typically denoted by the letters I, J, and K (in a three-dimensional model). In structured grids, data points are connected to their adjacent I, J, and K cells to form rectangular or cubic structures. Structured grids have cartesian, rectilinear, and curvilinear grids as the three common subtypes (DAAC, 2020).

The earliest and most basic type of structured grid is a cartesian grid, typically represented as an image or a matrix of equally spaced-out square or cube cells. In a cartesian grid, each pixel has a uniform size mapping into a simple XY grid; a digital image is a typical example of a cartesian grid. Uniform spacing, rectangular, easy cell neighbor search, distance, volume, and directional uniformity are valuable properties of cartesian grids. However, the major drawback of a cartesian grid is its inability to represent a non-square image. Increasing grid resolution is a simple way to resolve this, but the fundamental problem persists.

A rectilinear grid also has a rectangular matrix arrangement of data like the Cartesian grid but does not have a uniform spacing restriction. The basic unique properties of rectilinear grids include directional uniformity, partial distance uniformity, and absence of volume uniformity. Although rectilinear grids have a particular transform function that allows for varied grid cell size and density distribution, they can still not represent non-rectangular spaces (i.e., unable to digitize edges of curved or diagonal regions). Simulation of twisting water bodies like bays, estuaries, straits, etc.,

using rectilinear gridded models often faces inaccuracy problems (Sidoryakina, 2021; Sukhinov et al., 2019).

A curvilinear grid is similar to a rectilinear grid, but the cells are cuboids or quadrilaterals rather than rectangles or rectangular cuboids. Nonuniform direction, distance, and volume are unique features of curvilinear grids. A curvilinear grid is the only structured grid supporting non-rectangular/square spaces. Hence, cylindrical or spherical forms can be wrapped in a curvilinear grid to simulate or visualize their form accurately.

Unstructured grids, on the other hand, have arbitrary shapes and a set of general connectedness between points for each group of points. Unstructured grids lack restrictions on how they should be arranged, which gives them far more flexibility in defining complex structures. Non-orthogonal unstructured grids consist of triangles and quadrilaterals (2D) and tetrahedra, pentahedral (prisms), and hexahedra (3D). Thus, quadrilaterals and hexahedra can form an unstructured grid, but there are no restrictions on how many edges can share a node. However, storing and retrieving data in unstructured grids, like neighbor connectivity lists, demands more information compared to structured grids. Changes in element types and sizes can heighten numerical approximation errors, impacting accuracy, especially for one-dimensional flow disturbances due to the lack of parallel faces in tetrahedral elements (FLOW-3D, 2023).

Another emerging grid type is the specialty grid, which combines several structured and unstructured grids. Specialty grids are further separated into multiblock and hierarchical grids. Typically, they highlight aspects like multi-resolution or hierarchical information. However, one significant challenge with the specialty grid is the difficulty in managing the multi-block nature of the data (DAAC, 2020). The various types of grids are illustrated in Figure 1.

Multiblock grids are grid structures composed of unions of non-overlapping blocks, where each block functions as an independent grid, often of simpler rectilinear grid types, each with its sub-grid, and they interact through interpolation (DAAC, 2020; Rantakokko, 2000). These blocks can vary in size and resolution, and their combination forms the overall grid. When grids overlap, it typically indicates a variant of the multi-block grid structure, often referred to as a hierarchical grid. The advantages of a multi-block grid approach are manifold: it conserves resources by avoiding a single large grid for the entire space, facilitates parallel processing as each processor can handle an individual block, and aids in data segmentation by allowing focused access to specific subsets. However, multiblock grids have their share of challenges. Discontinuities between blocks make it complex to compute interblock visualizations like Streamlines. Additionally, spaces between blocks may lead to enclosed areas that are technically within the grid's bounding box but not represented in any data sets, which can be problematic for accurate simulations (DAAC, 2020).

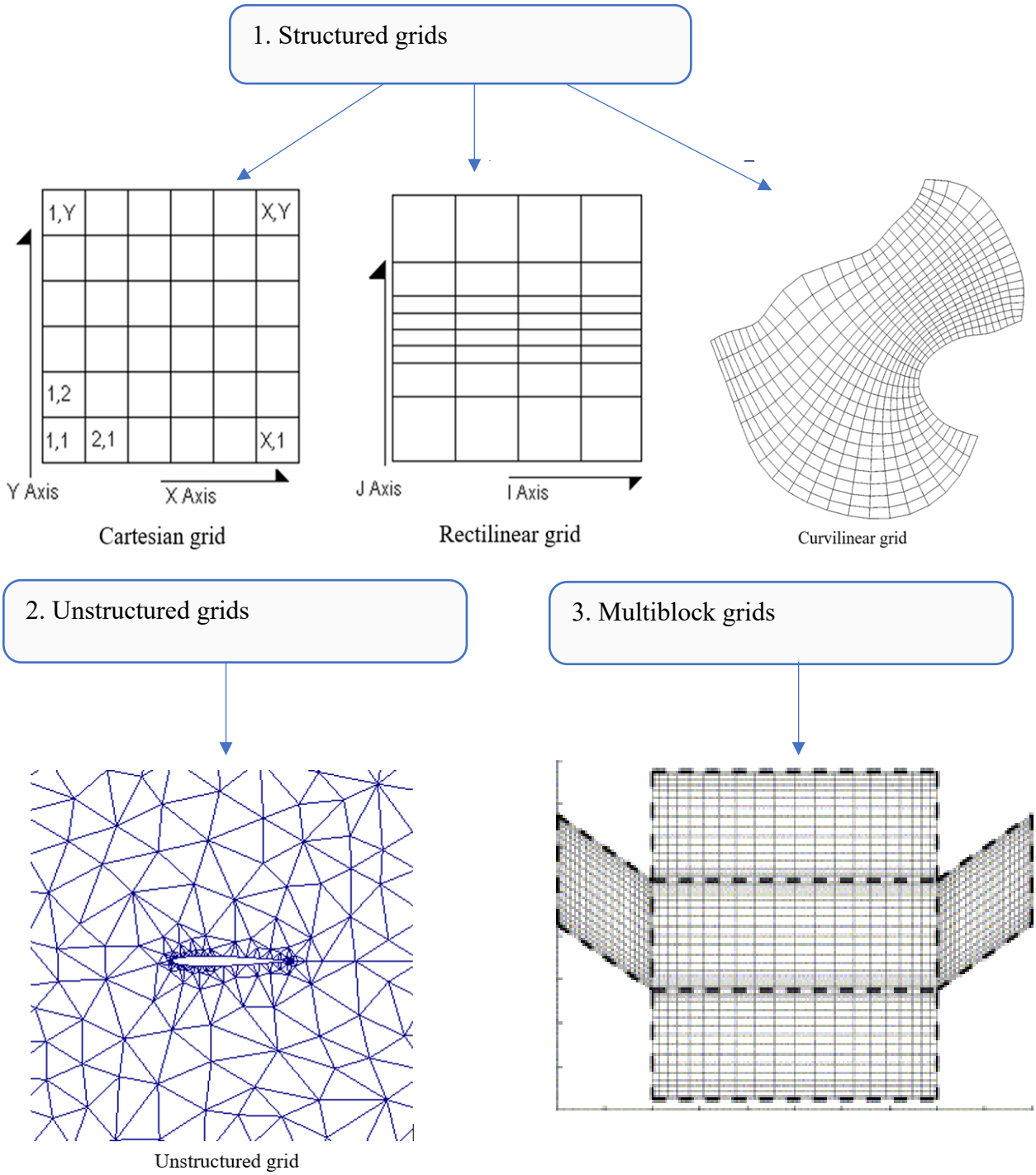

Figure 1: Example of 1) structured grids: cartesian and rectilinear grids (DAAC, 2020), curvilinear grid (Kate, 2006); 2) unstructured grid (DAAC, 2020) and 3) multiblock grid (Rantakokko, 2000).

Recent studies have adopted curvilinear grids in their hydrodynamic models for estuarine and coastal areas due to the efficiency of curvilinear grids in simulating hydrodynamic processes. In

addition, the curvilinear boundary-adaptive grid has been suggested to be applicable due to accurate mapping that fits complex geometries of estuaries and coastal regions and more precise simulation of the hydrodynamic processes in such regions (Sidoryakina, 2021; Sidoryakina & Sukhinov, 2017; Sukhinov et al., 2017, 2020).

Grid resolution influences the efficiency and accuracy of modeling hydrodynamics. Hence, it is necessary to use a suitable grid resolution in hydrodynamic models. Numerical grid resolution refers to the size of the grid cells. A finer grid resolution means the model can capture more minor features and details in the flow. A coarser grid resolution means that the model can only represent larger-scale features and may miss some smaller-scale processes. Models with finer resolutions require more cells to simulate the same area. Since calculations must be performed within each cell, finer resolutions require more calculations and an increased computational time.

1.5 Research Objectives

This study aims to investigate the impact of grid resolution on the efficiency and accuracy of modeling water surface elevation and salinity in Biscayne Bay (BB), Florida, using the EFDC+ model, which employs a curvilinear grid.

The specific objectives of this study are:

i. To develop five models in EFDC+ for BB with various resolutions: fine-resolution, medium-resolution, coarse2-resolution, coarse3-resolution, and coarse4-resolution.

ii. To evaluate the accuracy of the resolution models in simulating water surface elevation and salinity in BB, Florida, by comparing the model outputs with observational data.

iii. To provide recommendations on the appropriate grid resolution for modeling water surface elevation and salinity in BB, Florida, using the EFDC+ model based on the study's findings.

Chapter 2 Literature Review

This chapter aims to offer a comprehensive insight into hydrodynamic modeling, providing readers with a concise overview. The first section provides a succinct summary of recent research endeavors in hydrodynamic modeling. Additionally, the chapter delves into the impact of grid resolution on model outputs, offering a brief but insightful exploration of this crucial aspect within the realm of hydrodynamic modeling.

2.1. Review of Hydrodynamic Models

Various hydrodynamic models have been developed and used by many researchers, including the MIKE models, Princeton Ocean Model, TRIM-3D model, and Environmental Fluid Dynamics Code. The MIKE hydrodynamic models, developed by the Danish Hydraulic Institute (DHI), offer versatile tools and interfaces for setting up boundary conditions, bathymetry, and other factors in 2D or 3D hydrodynamic analyses. These models solve mass, momentum, salinity, and temperature equations, supporting various applications from environmental impact assessments to coastal flooding simulations. They employ parallelization techniques for optimized performance and can utilize graphical processing units (GPUs). Specifically, Marvin and Wilson (2016) used MIKE 21 and MIKE 3 models to simulate hydrodynamics between the Bay of Fundy and Salmon River. Also, Panda et al. (2010) applied MIKE11 and the artificial neural network model to simulate the river stage of the Kushabhadra branch of the Mahanadi delta. These models demonstrated good agreement with observed data.

The Princeton Ocean Model (POM), developed by Blumberg and Mellor (1987), is a robust free surface ocean model employing sigma coordinates. It also integrates turbulence and wave sub-models, along with the capability to handle wet-dry conditions. This model has been successfully applied in various water bodies, including river estuaries. Notably, the POM model has been

effectively used to simulate circulation patterns resulting from freshwater inflows in locations such as St. Andrew Bay (Beletsky & Schwab, 2001) and Lake Michigan (Blumberg & Kim, 2000). Similar to POM are the Estuarine, Coastal, and Ocean Model (ECOM), Navy Coastal Ocean Model (NCOM), and Finite Volume Coastal Ocean Model (FVCOM), which were developed in the late 1990s and 200s (Al-Zubaidi, 2016).

Casulli and Cheng (1992) developed the initial phase of TRIM-3D, a 3D model for shallow water flow. They derived its governing equations from the Navier-Stokes equations using turbulent averaging and assuming constant density and hydrostatic pressure. The model solves non-conservative forms of vertically averaged horizontal and vertical momentum equations, the free surface equation, and the continuity equation while considering dry/flood conditions and avoiding coordinate transformations. It incorporates wind and bottom stresses into momentum equations. TRIM-3D employs fixed staggered grids, a semi-implicit finite differences method, and a Eulerian-Lagrangian approach for convective terms. The model's stability hinges on horizontal viscosity. It produces two types of linear systems: tri-diagonal for horizontal velocities and penta-diagonal for the free surface equation. The model underwent verification and calibration in two case studies, including a simulation of the Lagoon of Venice in Italy, demonstrating efficient performance on Cray Y-MP8/432 in just 134 CPU seconds. Additionally, Casulli and Walters (2000) developed an unstructured grid version of this model called UnTRIM.

Several models have emerged based on the TRIM-3D model, with the Estuary, Lake, and Coastal Ocean Model (ELCOM) being one of the most prominent (Al-Zubaidi, 2016). Hodges and Dallimore (2006) developed the ELCOM, a three-dimensional system for hydrodynamics and water quality simulations in surface waters. It incorporates refinements for enhanced accuracy, scalar conservation, reduced numerical diffusion, and introducing a mixed-layer turbulence

closure scheme to compute vertical turbulent fluxes. This eliminates the need to solve tri-diagonal matrices for each water column. While hydrodynamic advection terms resemble the TRIM model, ELCOM employs a conservative third-order scalar transport method, ULTIMATE QUICKEST.

Environmental Fluid Dynamics Code Plus (EFDC+) (LLC, 2020), developed by Dynamic Solutions International, is a successor to the Environmental Fluid Dynamics Code (Hamrick, 1992). It is a popular 2D and 3D finite-difference surface water hydrodynamic model. EFDC+ model is based on the fluid continuity equation and comprises several integral sub-modules: (i) hydrodynamic module, (ii) water quality module, (iii) dye module, (iv) sediment transport module, (v) toxics module, (vi) waves module, (vii) Lagrangian particle tracking module, (viii) propeller wash, and (ix) marine hydrokinetics module. This tool is useful for comprehending and predicting environmental fluid flows, encompassing the transport and mixing of dissolved or suspended materials, as well as modeling the movement of pollutants and pathogenic organisms from both point and non-point sources (Cunanan & Salvacion, 2016; Wang et al., 2014). This three-dimensional surface water modeling system finds application in simulating hydrodynamics and reactive transport across various environments, including rivers, lakes, reservoirs, wetlands, estuaries, and coastal areas (Cunanan & Salvacion, 2016; Hamrick & Mills, 2000). Many researchers have successfully used it to simulate water levels (Liu et al., 2008), flows (Chen et al., 2016; Devkota & Fang, 2014, 2015; Liu & Garcia, 2008), salinity (Alarcon et al., 2022; Devkota & Fang, 2014; Jeong et al., 2010; Z. Liu et al., 2008; Xia et al., 2011), temperature (Chen et al., 2016; Devkota & Fang, 2014; Z.; Liu et al., 2008; Xia et al., 2011), and water quality (Hua & Zhang, 2017; Xia et al., 2011; Yin & Seo, 2016) based on physical principles in rivers, lakes, and estuaries. EFDC+ has a user-friendly graphical user interface and mesh developer.

EFDC+ was chosen as the preferred hydrodynamic and water quality simulation tool for St. Louis Bay due to its comprehensive development. The selection is supported by several advantageous features, including a user's manual and algorithm documentation, compatibility with various computer platforms, including PCs, and a history of successful applications in estuary systems. Moreover, EFDC+ offers the convenience of Grid+ sub-software, facilitating easier grid generation. Hashim (2001) also argued that EFDC+ exhibits faster simulation time performance than other models with similar data input.

2.2. Effect of Grid Resolution on Model Results

Several hydrodynamic model studies have explored the effects of model resolution on circulation patterns. Putman and He (2013) used the Global Hybrid Coordinate Ocean Model to investigate how the resolution of ocean models affects the accuracy of predictions of long-distance dispersal of marine organisms. They utilized particle tracking simulations to simulate the dispersal of virtual larvae in the ocean and examined how the resolution of the ocean model affected the resulting trajectories. The authors found that the resolution of the ocean model had a significant impact on the simulated particle trajectories and that particle tracking simulations conducted using ocean circulation models with greater resolution could better replicate the observed trajectories of near-surface drifters compared to simulations carried out using lower resolution models. Putman and He (2013) further suggested that ocean circulation models with high spatial and temporal resolution are crucial for areas near the coast where the main drivers of ocean circulation experience quick transitions.

Similarly, Andrejev et al. (2011) used a three-dimensional hydrodynamic model to assess the influence of spatial resolution on marine transport risk assessment. They investigated the Gulf of Finland in the Baltic Sea, a region heavily trafficked by ships and vulnerable to oil spills. They

used various model resolutions and compared the results to see how the resolution affects oil spill trajectories and concentrations. Their findings showed that the higher the resolution of the model, the more accurate the predictions of oil spill trajectories and concentrations. However, a higher-resolution model requires more computational resources, which can limit its feasibility.

Colberg et al. (2020) developed and assessed two ocean models with different spatial resolutions for the Great Barrier Reef region of Australia. The higher-resolution model had a grid spacing of approximately 0.5 km, while the medium-resolution model had a grid spacing of approximately 4 km. The models were run for a period of 10 years, and their outputs were compared to in-situ measurements and satellite data. Their findings showed that the higher resolution model provided more accurate representations of the ocean dynamics and biogeochemical processes in the region, particularly in the nearshore areas, while the medium resolution model was more efficient in terms of computational resources.

Also, Altenau et al. (2017) investigated the effects of spatial resolution and dimensionality on modeling hydraulics in a multichannel river at the regional scale. They developed two different hydrodynamic models, a 1D model and a 2D model, and used them to simulate the flow dynamics of the river at different spatial resolutions. Their study suggested that the 2D model fine-resolution model is more accurate in capturing the spatial variability of flow and water levels, while the 1D model is more computationally efficient.

In a study of the impact of mesh resolution on hydrodynamic simulations in coral reef environments, Saint-Amand et al. (2023) used a high-resolution hydrodynamic model to simulate a coral reef environment with varying mesh resolutions from coarse (4 km) to fine (0.25 km). They then evaluated the results of the simulations, specifically the flow patterns and water velocities,

and compared them with observations. The study found that fine mesh resolutions significantly improved the model's ability to accurately represent the flow patterns and velocities in the coral reef environment; hence, such an environment requires a model resolution finer than the reef scale. However, they also noted that finer resolutions require more computational resources and may not always be necessary.

Bracco et al. (2015) examined the submesoscale circulation in the Northern Gulf of Mexico and its impact on dispersion over the continental slope. They used two horizontal grid resolutions, 5 km and 1.6 km simulation with a Regional Ocean Modeling System (ROMS) model to study the submesoscale features and their effects on the dispersion. The study suggests that the submesoscale features play a crucial role in determining the dispersion patterns in the region and that high-resolution simulations are necessary to capture these features accurately. They also found that the representation of the topography and the stratification of the water column are critical factors in determining the dispersion patterns. In a related study, Bracco et al. (2018) investigated the effects of vertical and horizontal resolution on the representation of tracer dispersion along the continental slope in the northern Gulf of Mexico using a high-resolution numerical model. They found that vertical resolution has a more significant impact on the model performance than horizontal resolution, as it affects the mixing processes that control the tracer dispersion.

Conversely, Jarihani et al. (2015), from their satellite-derived digital elevation model (DEM) selection, preparation, and correction for hydrodynamic modeling study, found that the relationship between model performance and grid size demonstrated a non-linear response. Although hydrodynamic model results showed only slight improvement with smaller grid sizes (≤120 m), they stated that the enhancements came at considerably higher computational costs when compared to the 120 m, 250 m and beyond. However, grid sizes of 1000 m and 2000 m led

to a diminishing model accuracy. Also, Horritt and Bates (2001) in their spatial resolution for flood study ranging from 10 to 1000 m grid size, found that employing model grid sizes smaller than 100 m does not improve the results but does extend computational time.

Chapter 3 Materials and Methods

3.1 Description of Study Area

Biscayne Bay stretches south from a location between North Miami Beach and Sunny Isles Beach to the Arsenicker Keys and the Cutter Bank just to the east of those islands (Figure 2). It is located on the Atlantic coast of South Florida, the USA, at a latitude of 25° 35' 49.02" N and a longitude of 80° 15' 50.58" W; and is around 97 km long, up to 13 km broad, and has a surface area of 700 km^2. The Florida mainland borders the Bay on its western side. The Bay is connected to the Atlantic Ocean through several channels, including Government Cut, the main shipping channel for the Port of Miami, and is separated from the Atlantic Ocean to the east by a swath of barrier islands in the north, a sizable shoal in the center, and the northernmost Florida Keys in the south. The Bay is an important economic resource for the region, providing opportunities for fishing, boating, and other recreational activities. The area surrounding the Bay is also home to several parks and protected areas, including Biscayne National Park, which is one of the largest marine parks in the National Park system.

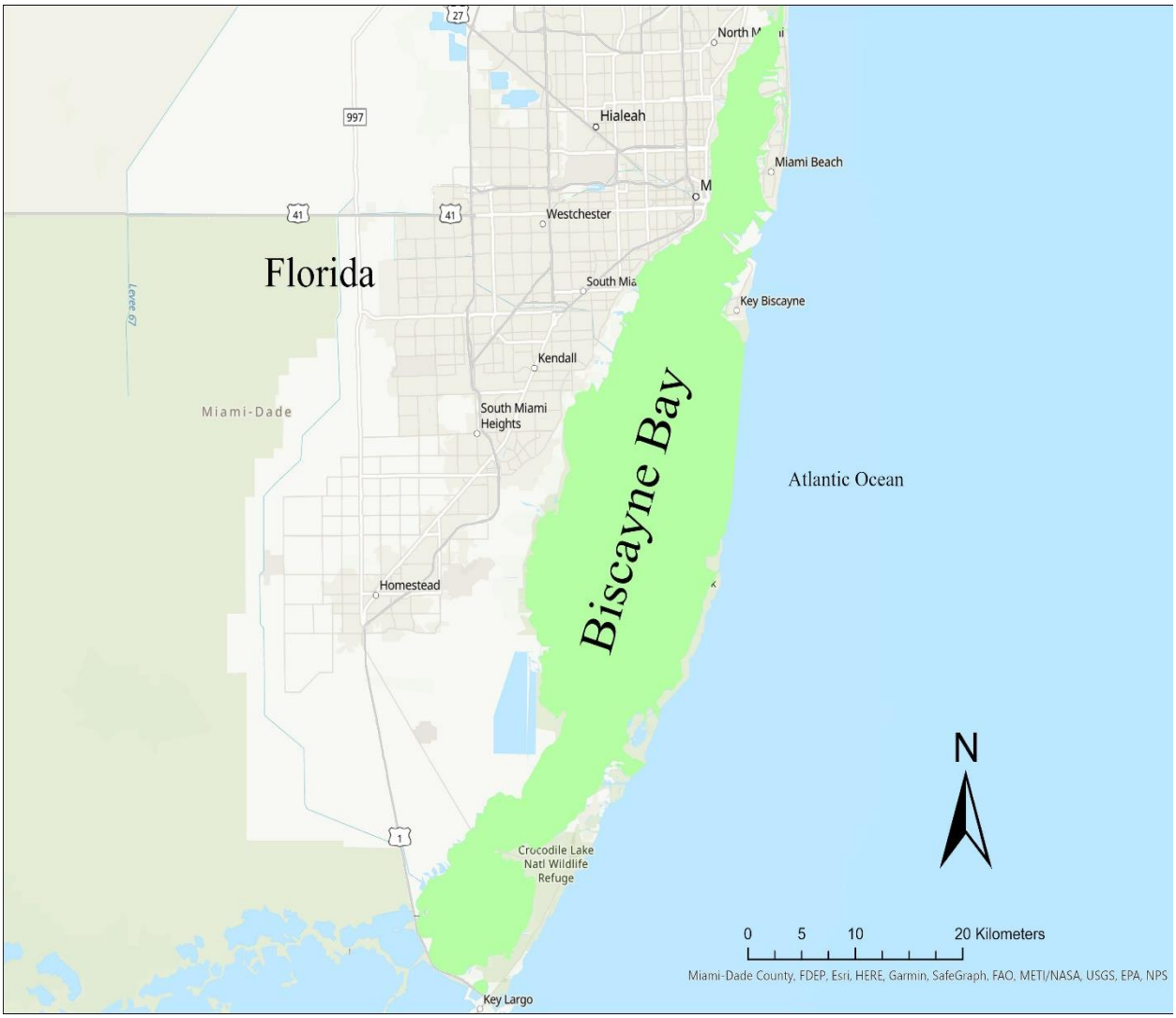

Figure 2. Study area, Biscayne Bay

3.2. Input Data and model setup.

This study involves setting up five models with five resolutions (fine-resolution, medium-resolution, coarse2-resolution, coarse3-resolution, and coarse4-resolution) following similar procedures. These models are based on the model setup by Alarcon et al. (2022). However, these models use curvilinear grids instead of a rectilinear grid.

3.2.1. Bathymetry

The hydrodynamic models were constructed using bathymetric data from the 1/3 arc-second Mean Lower Low Water bathymetric DEM developed by NOAA's National Ocean Service (NCEI, 2018). This data set utilizes hydrographic survey information specific to Biscayne Bay. The bathymetric data, presented as a NETCDF data cube in NAVD, was downloaded, geo-processed, and projected onto UTM coordinates (Zone 17 North, WGS84) on ArcGIS Pro. The resultant data raster has a horizontal spatial resolution of 20 m x 20 m and a vertical accuracy of 0.01 m to suit the fine-resolution model. In addition, the bottom roughness data used were exported in '.xyz' data format from Alarcon et al. (2022).

3.2.2. Obtaining existing model setup

Apart from bathymetry that was freshly downloaded and geo-processed as described in section 3.2.1., other input data for the models, including water level, flow, salinity, water temperature, and atmospheric data between January 2012 and December 2018, were obtained from Alarcon et al. (2022). According to Alarcon et al. (2022), the water level data were obtained from the Virginia Key Station of the NOAA's Tides & Currents Meteorological Observations Website (NOAA, 2022). The water flow and salinity data were obtained from the South Florida Water Management District (SFWMD) Environmental Monitoring Website (SFWMD, 2022). Tidal water temperature data were obtained from NOAA Virginia Key Station (NOAA, 2022), while canal water temperature data were obtained (SFWMD, 2022). The input data and the boundary conditions to each of the five resolution models was made to be closely similar to that of Alarcon et al. (2022). More information about these data is shown in Table 1. Figure 4 illustrates the various boundary conditions (BC) and the water level and salinity input data source stations for the models.

3.2.3. Development of grid resolutions

This study uses an arbitrarily generated medium-resolution model grid which consists of a finer resolution (~130 m × 130 m) in the North BB (i.e., from the Miami River to the Haulover area) and a coarser resolution (~300 m × 300 m) in the Central and South BB (i.e., from the Miami River to the Eagle Key) both joined together. The medium-resolution model grid was used as the base model to develop other resolution models. The medium-resolution model grid was generated using the Grid+ grid generation, version 1.0. The fine-resolution model was developed by dividing the "i-direction" and "j-direction" of the medium-resolution model grid by a factor of 2. In contrast, the coarse2-resolution model grid was developed by multiplying the "i-direction" and "j-direction" of the medium-resolution model grid by a factor of 2. Furthermore, a coarse3-resolution model grid was developed by multiplying the "i-direction" and "j-direction" of the medium-resolution model grid by a factor of 3, while a coarse4-resolution model grid was developed by multiplying the "i-direction" and "j-direction" of the medium-resolution model grid by a factor of 4. The models adopted the WGS 84 UTM zone 17N coordinate system and used meters as the unit of measurement. Figure 3 shows the configurations of the model grid resolutions for BB. Table 2 shows the general features of the grids for the five resolution models.

3.2.4. Running the models

The simulations were performed for a 24-month period, commencing on January 1, 2017, and concluding on December 31, 2018. To assess the outcomes derived from the EFDC simulation, the period from 01/01/2017 00:00 (January 2017) to 06/30/2017 23:00 (end of June 30, 2017), was designated as the warm-up phase, while the span from July 1, 2017, to December 31, 2018, was employed to assess the model's performance by comparing data collected from measurement stations with the model-generated data. The available field measurements for the WSE and Salinity

start on January 1, 2017, at 00:00:00 and end on December 31, 2018, at 23:59:00, for all the stations. The data output from the model was extracted to align with the times of available measured data for the analysis.

EFDC+ has three different time-step settings: the pre-processing time steps for input data, the internal dynamic time steps, and the post-processing time steps for output. In this study, the temporal resolution (time step) for measured data and model output is 1 hour (60 minutes). The models uniformly used an internal dynamic time stepping of 0.05 sec. initial value, 0.15 safety factor, 5 growth steps, and 30 sec. maximum time step. The five models were set uniformly and run independently, and their simulations were compared with one another and the observed data.

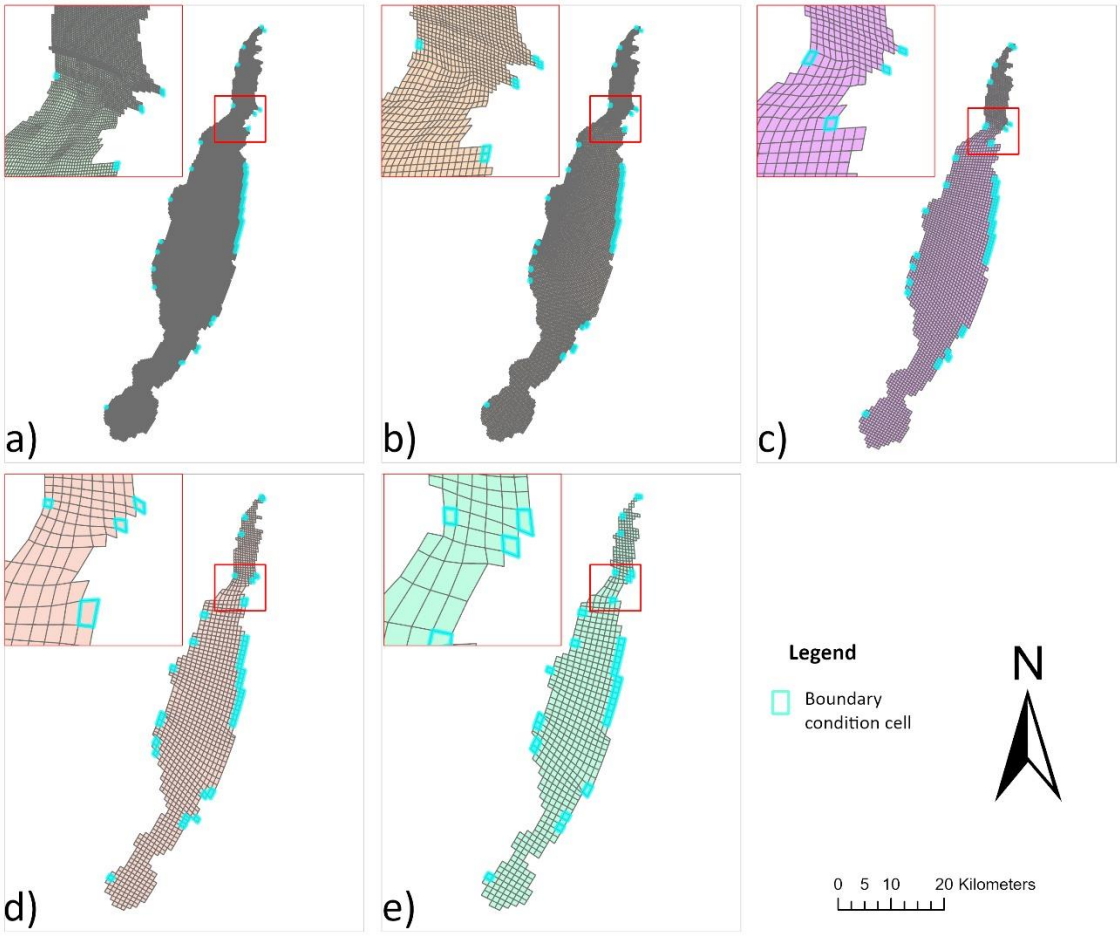

Figure 3. Grid configurations and average grid size for the (a) fine-resolution (130 m x 130 m), (b) medium-resolution (250 m x 250 m), (c) coarse2-resolution (500 m x 500 m), (d) coarse3-resolution (800 m x 800 m), and (e) coarse4-resolution (1000 m x 1000 m) models for BB on the same zoom level.

Table 1. Model boundary condition data and the stations from which the data was retrieved (Alarcon et al., 2022).

S/N	**Flow BCs Canals**	**Associated DBHYDRO Stations**	**Site**
Flow (m^3/s) & Canal Water Temperature (℃)			
1	Black Creek	S21_S	S21
2	Miami Canal	S26_S + S25_C (Average for Temperature)	S26 + S25 (Average for Temperature)
3	S20GS Canal	S20G_S	S20G
4	Mowrey Canal	S20F_S	S20F
5	Princeton Canal	S21A_S	S21A
6	Snapper Creek	S22_S	S22
7	Biscayne Canal	S28_S	S28
8	Little River Canal	S27_S	S27
9	Cutler Drain Canal	S123_S	S123
10	Aerojet Canal	S197_C	S197
11	Coral Gables Canal	G93	G93
13	Snake Creek	S29_S	S29
Salinity (ppt)			
1	Sal_New_BISCD8	BISCD8	BISCD8
2	Sal_New_BISC10B	BISC10B	BISC10
Water Level (m) & Tidal Water Temperature (℃)			
	Station	Datum	
	Virginia Key	NAVD	

Table 2. Grid features for the five resolutions

Grid Features	*Fine*	*Medium*	*Coarse2*	*Coarse3*	*Coarse4*
Model area (km^2)	698	706	695	655	616
Easting size (m)	30781.23	30844.40	30596.87	30370.87	30148.56
Northing size (m)	79495.72	79499.66	79281.85	78945.29	78220.50
Centroid Easting (m)	572478.31	572446.72	572322.96	572315.04	572310.29
Centroid Northing (m)	2825963.91	2825965.88	2826074.78	2826243.06	2826218.80
Centroid latitude	25.55°	25.55°	25.55°	25.55°	25.55°
Centroid longitude	-80.28°	-80.28°	-80.28°	-80.28°	-80.28°
Vertical grid type	Sigma stretch	Sigma stretch	Sigma stretch	Sigma stretch	Sigma stretch
Total grid cells	46542	11804	2870	1206	635
Total number of water column computational cells	93084	23608	5740	2412	1270
Average grid size	130 m x 130 m	250 m x 250 m	500 m x 500 m	800 m x 800 m	1000 m x 1000 m
Horizontal rows	738	371	187	126	94
Horizontal columns	152	78	40	27	21
Vertical layers	2	2	2	2	2
Approx. time to run for the 2 yr. period (hours)	240	27	4	0.9	0.8

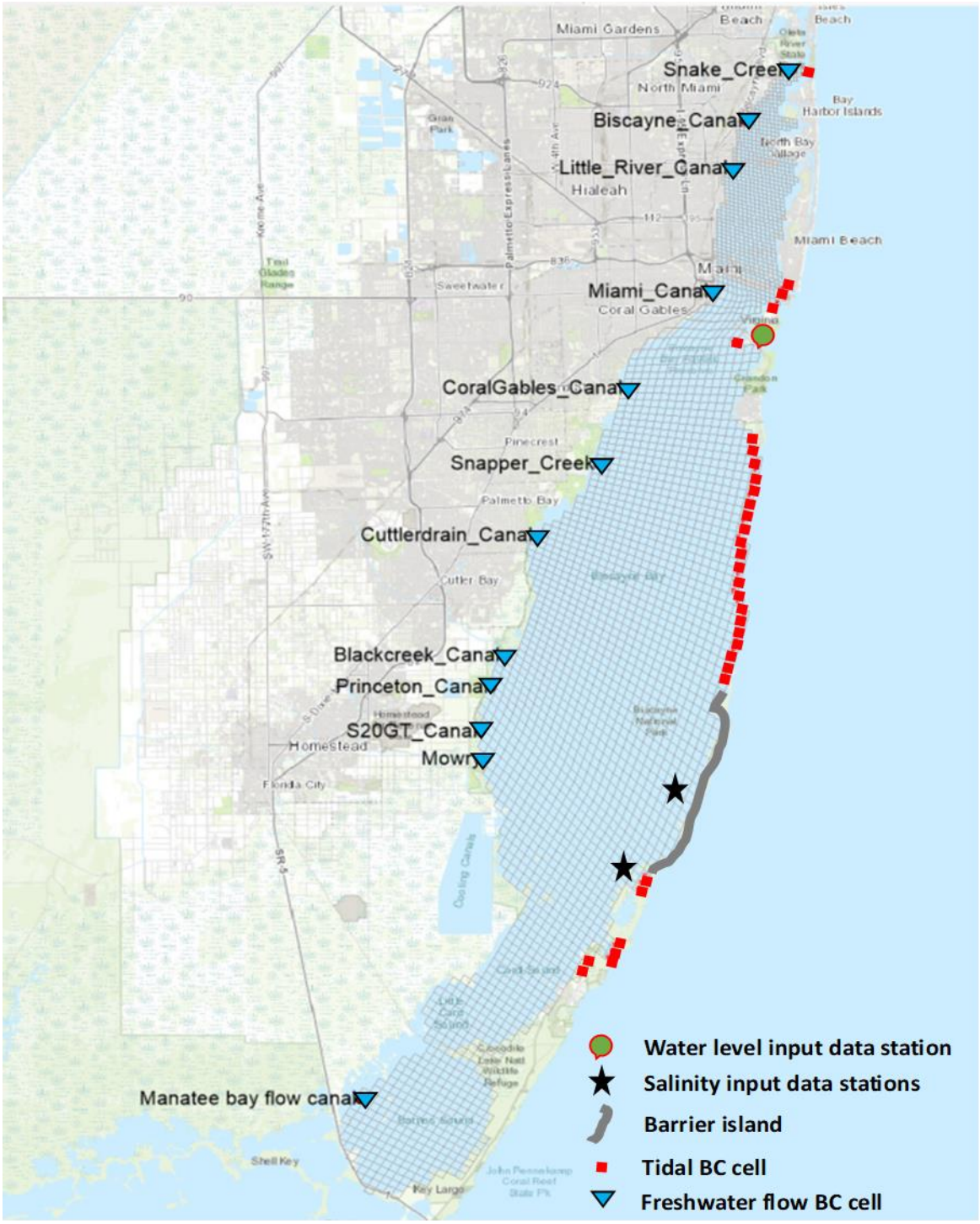

Figure 4. The boundary conditions and the water level and salinity input data source stations for the study overlaid on the medium resolution grid.

3.3. Statistical Indicators

Three statistical indicators of goodness of fit were used besides the time series comparisons between simulated and measured time series results. Their selection was based on related literature and their capabilities in judging model performances in hydrology and hydrodynamics. These statistics include the calculation of the coefficient of determination (R^2), RMSE-observations standard deviation ratio (RSR), and Kling-Gupta efficiency (KGE). The following section explains the methodology for computing each of these statistical indicators.

Coefficient of determination (R^2)

$$R^2 = \frac{[n\sum_{i=1}^{n} O_i P_i - (\sum_{i=1}^{n} O_i)(\sum_{i=1}^{n} P_i)]^2}{[n\sum_{i=1}^{n}(O_i)^2 - (\sum_{i=1}^{n} O_i)^2][n\sum_{i=1}^{n}(P_i)^2 - (\sum_{i=1}^{n} P_i)^2]}$$

…… (21)

RMSE-observations standard deviation ratio (RSR)

$$RSR = \frac{RMSE}{STDEV_{O_i}} = \left[\frac{\sum_{i=1}^{n}(O_i - P_i)^2}{\sum_{i=1}^{n}(O_i - \overline{O})^2}\right]$$

…… (23)

Kling-Gupta efficiency (KGE)

$$KGE = 1 - \sqrt{\left(\frac{\overline{P_i}}{\overline{O_i}} - 1\right)^2 + \left(\frac{STDEV_{P_i}}{STDEV_{O_i}} - 1\right)^2 + (R-1)^2}$$

…… (25)

where:

O_i represents observed data

P_i represents predicted data

$\overline{O_i}$ represents the mean of observed data

$\overline{P_i}$ represents the mean of predicted data

n represents the number of observations.

STDEV represents standard deviation

R represents the linear correlation between observations and simulations

Subsequently, statistics were computed based on the synchronized data sets for each site throughout the entire 2-year period.

The coefficient of determination, R^2 (equation 21), gauges the degree of alignment or correlation between the model and the observed data. In a perfect alignment scenario, where the model and observed data perfectly match, the R^2 value would be 1. Generally, $R^2 > 0.5$ is deemed acceptable for monthly time-step simulations (Moriasi et al., 2007).

RMSE-observations standard deviation ratio (equation 23) is a metric derived from the ratio of RMSE to the standard deviation of observed data. Unlike conventional error indices, RSR includes a normalization factor, allowing its applicability to diverse constituents. RSR values range from 0, representing perfect model simulation with zero RMSE, to higher positive values. A lower RSR signifies better model simulation performance.

Kling-Gupta efficiency (equation 25), as proposed by Gupta et al. (2009), is a metric that breaks down the Nash-Sutcliffe Efficiency (NSE) into its individual components, namely correlation, variability bias, and mean bias. This approach aims to overcome perceived limitations in NSE and has gained popularity for model calibration and evaluation. Like NSE, a KGE value of 1 signifies

a perfect agreement between model simulations and observations. While positive KGE values are often interpreted as indicative of "good" model performance and negative values as "bad," it's noteworthy that some authors do not explicitly specify KGE = 0 as the threshold between "good" and "bad" performance. Knoben et al. (2019) argue against relying on NSE interpretation to assess KGE values. Instead, they emphasize the importance of comprehending the individual components of KGE and using benchmark values for comparison to establish a new understanding of model performance based on this metric. Although the KGE metric has been widely adopted, there are ongoing opportunities for improvement, and exploring alternative ways to quantify model performance is encouraged. KGE values within the range of -0.41 to 1 suggest a better model performance compared to the mean observed value (Knoben et al., 2019).

Chapter 4 Results and Discussion

This chapter unveils the intricate details of our study on the effect of grid resolution on hydrodynamic modeling of estuarine water surface elevation and salinity, presenting the results, statistical analyses, and the discussion of our findings. It serves as a scholarly nexus by dissecting the multifaceted nature of the findings, exploring patterns, correlations, and implications to contribute an insightful discussion within the broader context of grid resolution effects on hydrodynamic modeling.

4.1. Water Surface Elevation (WSE)

Three measurement points for water surface elevation were employed to assess and compare the models' performances. These data were sourced from the Environmental Monitoring Website of the South Florida Water Management District (SFWMD, 2022). The three measurement points are all located at mouth of canals flowing into the Bay: the Miami River Station (MRMS4), the Cuttlerdrain Canal Station (S123_T), and the S20GT Canal Station (S20GT), to gain insights into the models' behavior in simulating the water level within the Bay (Figure 5a).

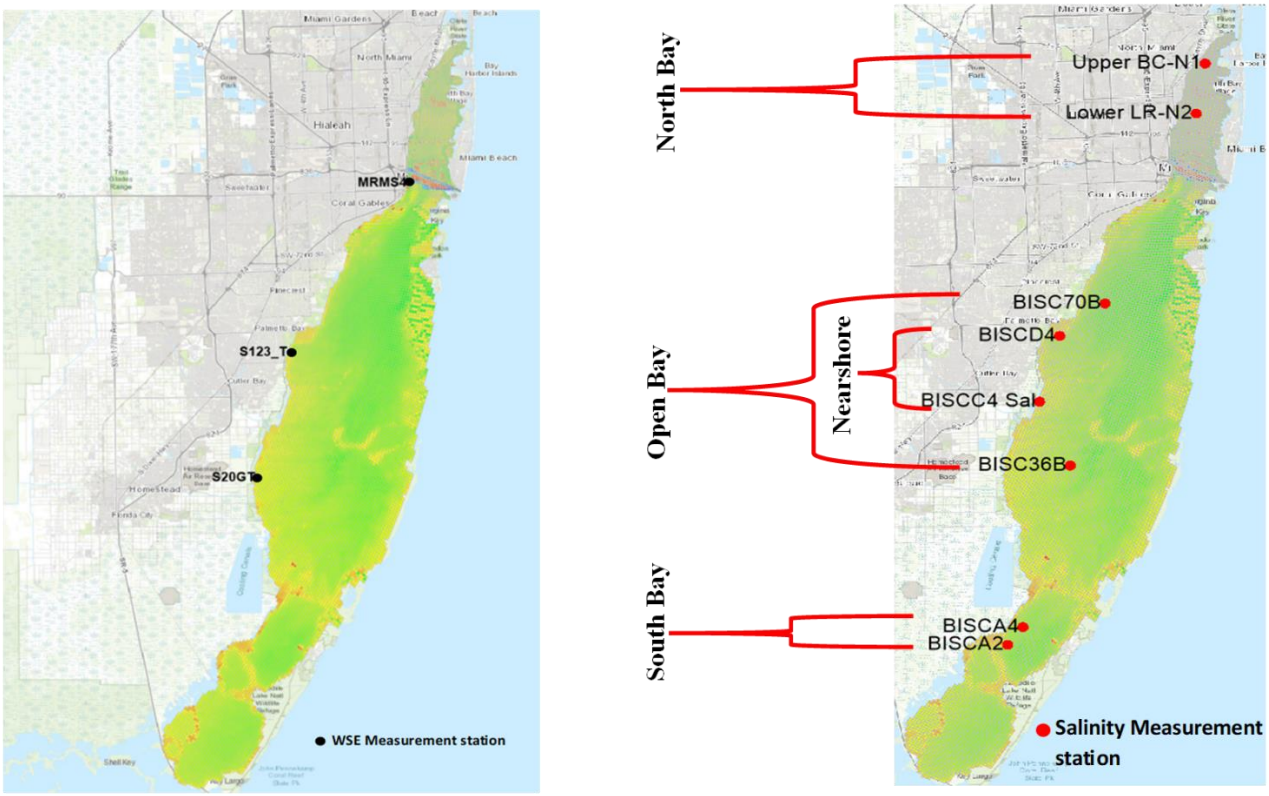

(a) (b)

Figure 5. a) The measurement points for water surface elevation overlaid on the medium-resolution grid; b) The Bay divisions and the salinity stations considered.

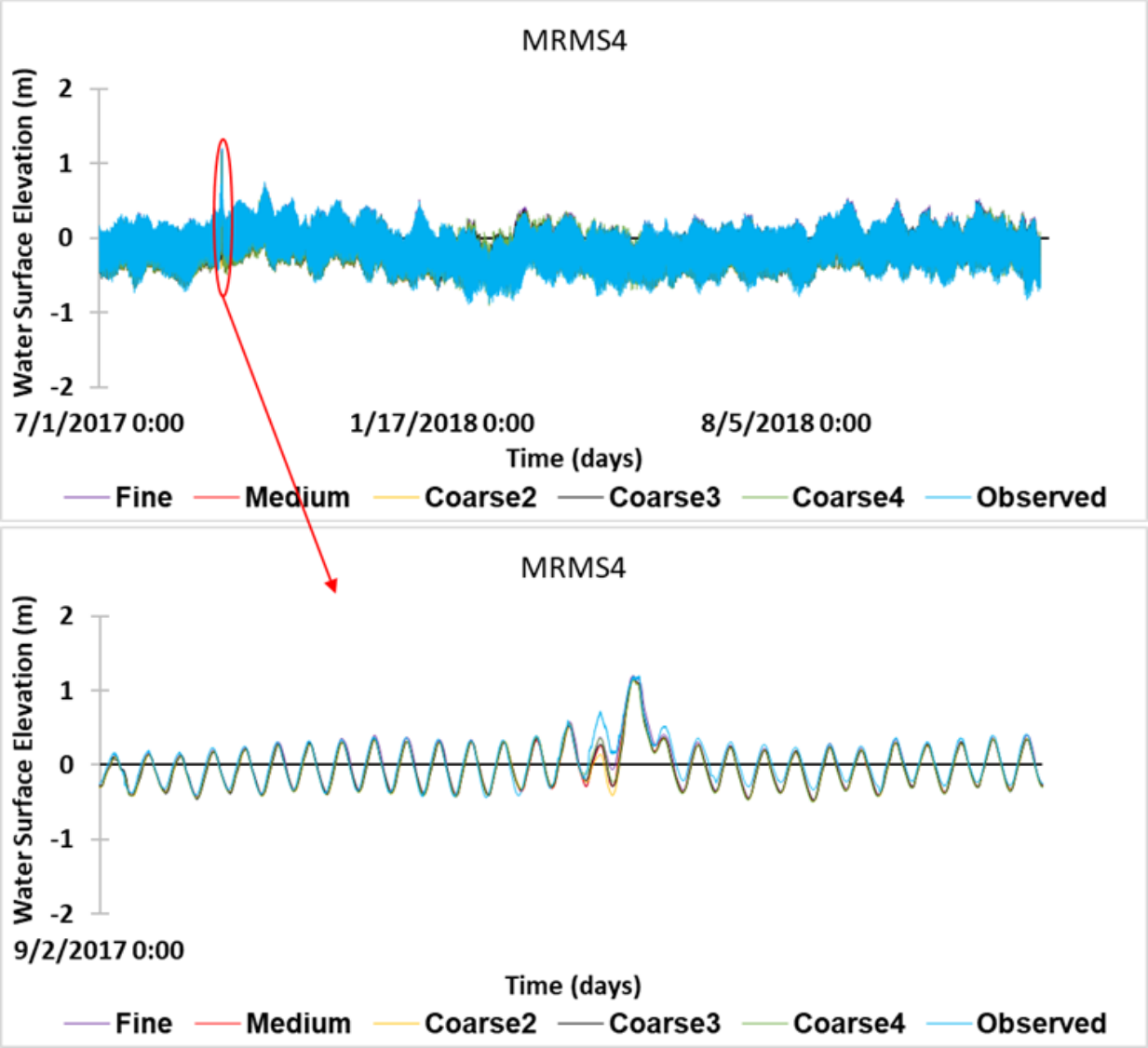

Figure 6a. MRMS4 Station time series plots for WSE

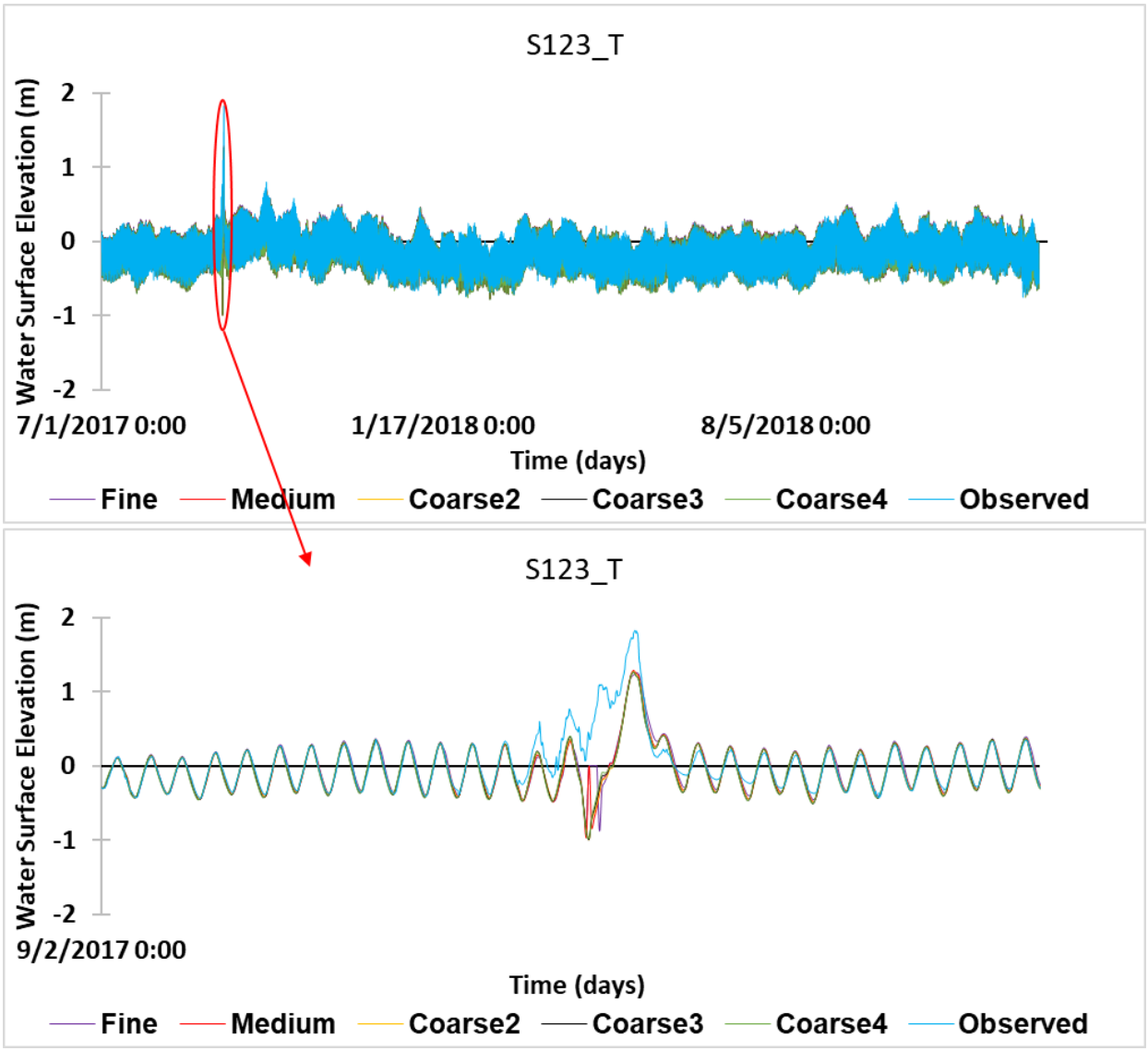

Figure 6b. S123_T Station time series plots for WSE

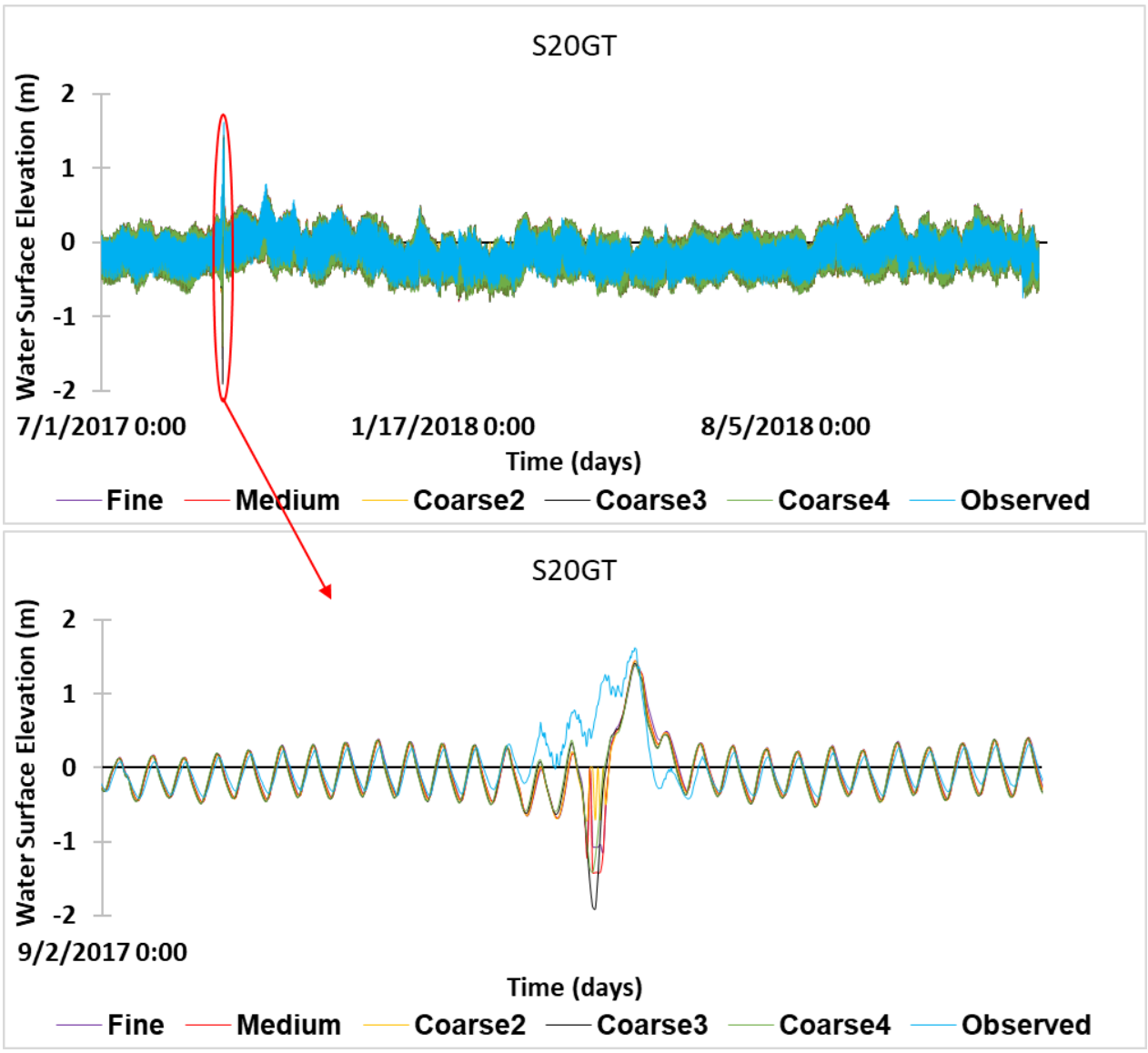

Figure 6c. S20GT Station time series plots for WSE

Figure 6 (a, b, and c) shows the time series plots for modeled and measured data at the three WSE measurement stations (MRMS4, S123_T, and S20GT). At the MRMS4 station, the difference between the average observed data (-0.137 m) and the Fine, Medium, Coarse2, Coarse3, and Coarse4 resolutions are -1.1 cm, 1.4 cm, 1.6 cm, 1.3 cm, and 1.7 cm, respectively. Also, a comparison between the average Fine resolution model simulation and the average simulations of

other models shows that they have similar performance with their differences ranging between 2.5 cm and 2.8 cm.

Similarly, at the S123_T station, the difference between the average observed data (-0.146 m) and the Fine, Medium, Coarse2, Coarse3, and Coarse4 resolutions are -0.1 cm, 1.0 cm, 1.2 cm, 1.5 cm, and 1.6 cm, respectively. In the same vein, a comparison between the average Fine resolution model simulation and the average simulations of other models shows that they have similar performance with their differences within the range of 1.0 cm and 1.7 cm.

At the S20GT station, the difference between the average observed data (-0.148 m) and the Fine, Medium, Coarse2, Coarse3, and Coarse4 resolutions are -0.4 cm, 1.2 cm, 1.3 cm, 1.7 cm, and 1.7 cm, respectively. In the same vein, a comparison between the average Fine resolution model simulation and the average simulations of other models shows that they have similar performance with their differences within the range of 0.8 cm and 1.4 cm.

Generally, the models followed similar trends and performed similarly. Specifically, the maximum difference between the average observed data and the simulated data for the models is 2 cm (~0.02 m) while maximum approximate difference between the average simulations of the models is 0.7 cm (~0.007 m). Therefore, the models were closer to each other than they were to the measured data.

Table 3 presents the statistical assessment for water surface elevation, including the coefficient of determination (R^2), RMSE-observations standard deviation ratio (RSR), and Kling-Gupta efficiency (KGE). Similarly, Figure 7 is a bar chart illustrating the statistical indicators across the different resolutions at different WSE stations, which shows a slight improvement in the performance trend of the models with an increase in resolution. It gives a visualization of the

statistical indicators presented in Table 3. The R^2, RSR, and KGE range between 0.91 – 0.94, 0.25 – 0.31, and 0.82 – 0.88, respectively, at the MRMS4 station. Similarly, the R^2, RSR, and KGE range between 0.90 – 0.93, 0.27 – 0.33, and 0.87 – 0.96, respectively, at the S123_T station. Also, a closer look at their respective performances shows that the Fine- and Medium-resolution models did slightly better in their simulation of the WSE with R^2 ranging between 0.921 – 0.943, RSR between 0.248 – 0.288, and KGE between 0.828 – 0.963 at MRMS4 and S123_T stations. On the other hand, the models generally performed poorer at the S20GT station. For instance, the R^2, RSR, and KGE range between 0.582 – 0.733, 0.584 – 0.779, and 0.685 – 0.807, respectively, with the Coarse4-resolution model having the least performance. Although the models performed within acceptable ranges, the slight decrease in the statistical indicators for the Coarse3 and Coarse4 models shows that coarser resolution can affect the model accuracy. This might be more evident if a larger factor is used to coarsen the medium resolution further.

A closer look at the storm event (Hurricane Irma) in 2017 shows more variation between modeled and measured data as well as between the different models. The models under-simulated WSE by about 0.2 – 1.5 m at the S123_T station between 9/9/2017 at 1:00 and 9/10/2017 at 4:00, but they were able to simulate the storm event better afterward (Fig. 6b). Similarly, there was a 0.4 – 2.0 m under-simulation of WSE at the S20GT station between 9/8/2017 at 20:00 and 9/10/2017 at 2:00, with a better simulation afterward (Fig. 6c). However, there was less difference observed for these periods at the MRMS4 station (Fig. 6a).

The model performed better at the MRMS4 and S123_T stations compared to the S20GT station (Table 3). This difference in performance may be due to the location of the WSE gauges. First, the MRMS4 station is located near the water level BC source station at Virginia Key (Figure 4).

Second, MRMS4 and S123_T are located directly across from open boundary tidal locations; however, S20GT is located west of a closed boundary (Figure 4).

The simulation utilized a single water surface elevation (WSE) boundary condition data from Virginia Keys, extending uniformly across the open boundary. Including an additional WSE boundary condition in the southern region may improve the accuracy and overall effectiveness of the representation of local dynamics and contribute to further improvements in WSE simulations.

Table 3. Error statistics for measured versus simulated water surface elevation.

Calibration Points	***Parameters***	***Fine Resolution***	***Medium Resolution***	***Coarse2 Resolution***	***Coarse3 Resolution***	***Coarse4 Resolution***
MRMS4	R^2	0.943	0.943	0.914	0.92	0.937
S123_T	R^2	0.928	0.921	0.917	0.914	0.9
S20GT	R^2	0.733	0.707	0.714	0.609	0.582
MRMS4	RSR	0.248	0.263	0.307	0.294	0.267
S123_T	RSR	0.271	0.288	0.293	0.303	0.327
S20GT	RSR	0.584	0.604	0.605	0.747	0.779
MRMS4	KGE	0.882	0.828	0.821	0.844	0.826
S123_T	KGE	0.963	0.9	0.889	0.871	0.868
S20GT	KGE	0.807	0.801	0.794	0.703	0.685

Figure 7: Bar chart illustrating the statistical indicators comparing measured and modeled WSE across the different resolutions and stations.

4.2. Salinity

To understand the impact of resolution on how the model simulates salinity distribution across the Bay, the Bay was divided into four regions: Nearshore, Open Bay, South Bay, and North Bay (Figure 5b). This method of division includes two measurement stations for each region, except for the North Bay division, which does not have a measurement station. The measured data from these stations are from SFWMD. The selected stations for the model performance assessment include BISCA2 and BISCA4 for the South Bay division, BISC36B and BISC70B for the Open Bay division, and BISCC4 and BISCD4 for the Nearshore division. Two points in North Bay (Upper BC-N1 and Lower LR-N2) were selected to compare the performances of the five models (Figure 5b).

Figure 8 shows the time series plots of modeled and measured data for the six salinity measurement stations (BISCA2, BISCA4, BISC36B, BISC70B, BISCC4, and BISCD4). Generally, the models have no trends when simulating salinity. Specifically, the models performed better at four stations, including Open Bay (BISC36B and BISC70B), South Bay (BISCA2 and BISCA4), and poorer at Nearshore (BISCC4 and BISCD4). BISC36B, BISC70B, BISCA2, and BISCA4 have close average salinities with each other and the observed data. At BISCC4, the Coarse3 and Coarse4 models over-simulated the observed data with an average value of 10 and 11 ppt, respectively. Similarly, at BISCD4, the Coarse3 and Coarse4 models over-simulated the observed data with an average value of 6 and 7 ppt, respectively.

At the nearshore stations, BISCC4 and BISCD4, the models performed better in simulating the salinity when the observed salinity was relatively high (15 ppt and above) and underperformed when the salinity dropped below 15 ppt. At the remaining measurement stations, BISC36B,

BISC70B, BISCA2, and BISCA4, the models had a similar performance with small differences and a closer match with the observed data.

The freshness of the BISCC4 and BISCD4 stations could be attributed to the nearshore location, which is near the mouth of the freshwater canals, and it is evident that models were unable to simulate low salinity levels of about 10 ppt and below at BISCC4 and low salinity levels of about 20 ppt and below at BISCD4. Secondly, the farther distance of the BISCC4 and BISCD4 from the tidal BCs may be the reason for the relatively low performance of the models. On the other hand, the BISC36B and BISC70B are located within the Open Bay section and are somewhat closer to the tidal BCs.

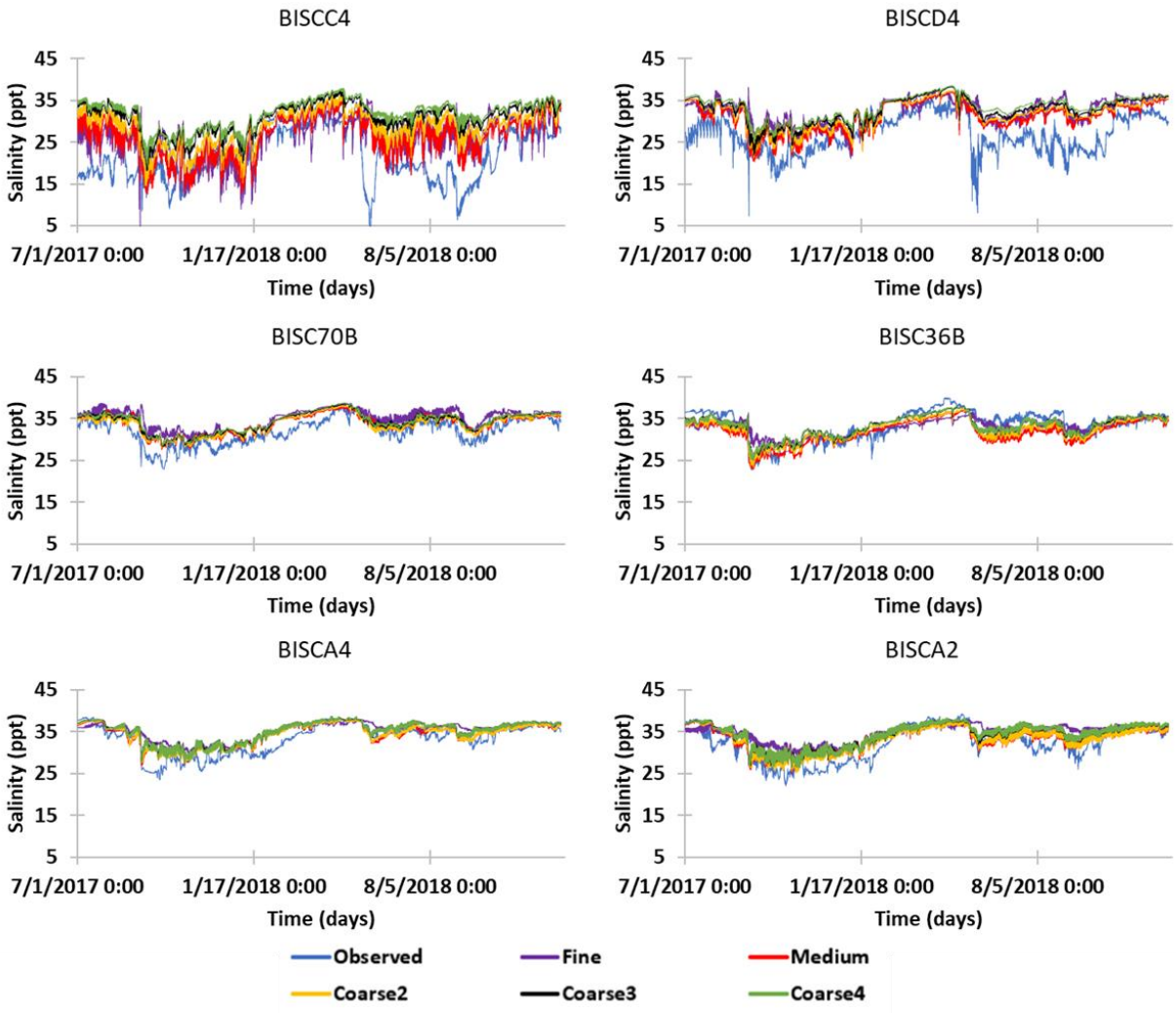

Figure 8. Time series plots for BISCA2, BISCA4, BISC36B, BISC70B, BISCC4, and BISCD4 salinity stations.

Table 4 displays the statistical assessment results for salinity for the six stations selected in the South Bay, Open Bay, and the Nearshore Division. Similarly, Figure 9 is a bar chart illustrating the statistical indicators across the different resolutions at different salinity stations. The R^2, RSR, and KGE analyses of the models across the six salinity stations (BISCA2, BISCA4, BISC36B, BISC70B, BISCC4, and BISCD4) showed that the models performed similarly and better at the South Bay (BISCA2 and BISCA4) and the Open Bay (BISC36B and BISC70B) stations with a

minimum R^2 of 0.649, maximum RSR of 1.094, and minimum KGE of 0.492. Conversely, the R^2, RSR, and KGE across the models at the nearshore stations (BISCC4 and BISCD4), are relatively low. For instance, at the nearshore stations, the R^2 value got as low as 0.142, the RSR as high as 1.663, and the KGE as low as 0.213. This shows that the model performed similarly within each region (nearshore, south, open Bay). In other words, the models performed similarly at stations within the same Bay division than those in different Bay divisions.

Table 4. Error statistics for measured versus simulated salinity in the BISCA2, BISCA4, BISC36B, BISC70B, BISCC4, and BISCD4 stations.

Bay Section	*Calibration Points*	*Parameters*	*Fine Resolution*	*Medium Resolution*	*Coarse2 Resolution*	*Coarse3 Resolution*	*Coarse4 Resolution*
Open Bay	**BISC70B**	R^2	0.649	0.745	0.734	0.767	0.761
Open Bay	**BISC36B**	R^2	0.686	0.735	0.433	0.769	0.775
Nearshore	**BISCD4**	R^2	0.27	0.42	0.433	0.452	0.463
Nearshore	**BISCC4**	R^2	0.142	0.285	0.23	0.239	0.726
South Bay	**BISCA4**	R^2	0.737	0.783	0.813	0.82	0.82
South Bay	**BISCA2**	R^2	0.695	0.769	0.789	0.801	0.796
Open Bay	**BISC70B**	RSR	1.094	0.747	0.727	0.832	0.863
Open Bay	**BISC36B**	RSR	0.661	0.67	0.819	0.516	0.514
Nearshore	**BISCD4**	RSR	1.496	1.246	1.349	1.515	1.663
Nearshore	**BISCC4**	RSR	1.236	1.168	1.468	1.777	0.659
South Bay	**BISCA4**	RSR	0.779	0.582	0.549	0.716	0.682
South Bay	**BISCA2**	RSR	0.915	0.634	0.586	0.743	0.743
Open Bay	**BISC70B**	KGE	0.66	0.701	0.71	0.715	0.718
Open Bay	**BISC36B**	KGE	0.489	0.734	0.255	0.668	0.663
Nearshore	**BISCD4**	KGE	0.406	0.553	0.527	0.514	0.46
Nearshore	**BISCC4**	KGE	0.317	0.439	0.311	0.213	0.833
South Bay	**BISCA4**	KGE	0.555	0.699	0.717	0.678	0.709
South Bay	**BISCA2**	KGE	0.492	0.664	0.688	0.66	0.681

Figure 9: Bar chart illustrating the statistical indicators across the different resolutions at salinity stations.

Generally, the salinity simulations across the stations and resolutions did not follow a linear or regular trend. For instance, although the South Bay (BISCA2 and BISCA4) and the Open Bay (BISC36B and BISC70B) stations had a minimum R^2 of 0.649, maximum RSR of 1.094, and minimum KGE of 0.492, it did not mean that the Fine resolution consistently performed best or worst across the stations so also other resolutions. Also, at the nearshore stations where the R^2 value got as low as 0.142, the RSR as high as 1.663, and the KGE as low as 0.213, there is no resolution model that consistently maintains a particular performance trend (better or poorer).

Simulations in the North Bay can only be compared to each other and not to observed data since there are no measurement stations in the North Bay. The simulated salinity plots in the North Bay behaved similarly but there existed some divergence across the resolutions (Figure 10). This divergence is more pronounced for Coarse3 and Coarse4 models, which diverged from other model simulations by about 5 ppt on average in the North division, while the Central, South, and Nearshore divisions never exhibited such divergence among the resolutions. The divergence across resolutions at each station is greater in the North compared to that seen at the stations in the Central, South, and Nearshore divisions where little divergence of less than 0.5 ppt was observed at some stations and times. At the Upper BC-N1 point, the average simulated data for Fine, Medium, and Coarse2 models are 31.36, 30.58, and 30.32 ppt, respectively; in contrast, the Coarse3 and Coarse4 models have relatively low average simulated data of 25.76 and 21.88 ppt, respectively. Similarly, at the Lower LR-N2 point, the average simulated data for Fine, Medium, Coarse2, Coarse3, and Coarse4 models are 33.21, 31.83, 30.29, 29.96, and 24.76 ppt, respectively.

In the comprehensive analysis of simulated salinity data across various resolutions and points, it becomes evident that the Fine resolution model for Lower LR-N2 exhibits a marked divergence in average values compared to the Upper BC-N1 simulations. Specifically, the absolute differences

in average salinity data highlight distinctive disparities of approximately 2.0 ppt, 1.3 ppt, 0.03 ppt, 4.2 ppt, and 2.9 ppt for Fine, Medium, Coarse2, Coarse3, and Coarse4, respectively. Further examination reveals noteworthy variations ranging from 0.8 to 9.5 ppt at Upper BC-N1 and 1.4 to 8.5 ppt at Lower LR-N2, underscoring the significance of the Coarse3 and Coarse4 models in exhibiting distinct performance characteristics compared to the Fine, Medium, and Coarse2 models at these specific points.

No strict conclusion regarding salinity can be made in the North Bay since there is no observed data to confirm which model did better than other models. This calls for establishing some measurement stations in the North Bay. This is especially important considering the complex geometry and possible complex dynamics existing therein.

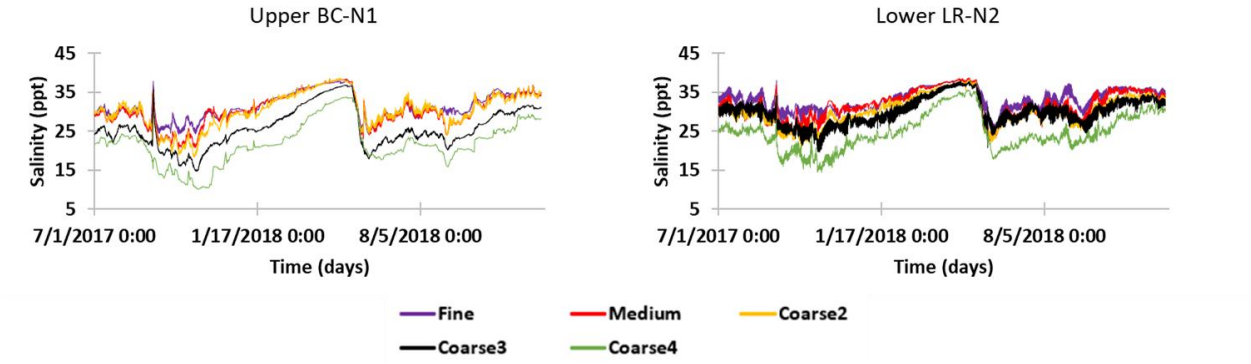

Figure 10. Time series plots for Upper BC-N1 and Lower LR-N2 points

An intriguing trend emerges as WSE demonstrates a slight improvement with increasing resolution, whereas salinity exhibits no such relationship between the model performance and their resolutions, under the same conditions. This slight improvement of models' WSE simulation with increasing resolution might result from the location of the tidal boundary data obtained directly from the Virginia Key open boundary to the Atlantic Ocean. In contrast, the irregular fashion in

the salinity simulation might also be related to the location of the salinity BC data behind the barrier island instead of the open boundary of the domain with the Atlantic Ocean.

The limitations of this study are 1) the boundary condition salinity data used for setting up more than two-third of the salinity BC cells were measured behind a barrier island instead of the direct inlet from the Atlantic Ocean (figure 4); and 2) there were no salinity measurements for the North Bay assessment. Better results would likely be achieved if the tidal salinity boundary condition data were obtained in an area closer to the Atlantic Ocean open boundary instead of the current location behind the barrier island.

Chapter 5 Conclusion

5.1 Summary of project and methods

Five Environmental Fluid Dynamic Code Plus (EFDC+) resolution models, including Fine, Medium, Coarse2, Coarse3, and Coarse3 resolutions, were developed. The Grid+ software was used to generate curvilinear grids, which were used to develop the models. The medium-resolution model grid, which was used as the base model to develop other resolution models, consists of a finer resolution (~130 m × 130 m) in the North BB (i.e., from the Miami River to the Haulover area) and a coarser resolution (~300 m × 300 m) in the Central and South BB (i.e., from the Miami River to the Eagle Key) both joined together. The fine-resolution model was developed by dividing the "i-direction" and "j-direction" of the medium-resolution model grid by a factor of 2. In contrast, the Coarse2, Coarse3, and Coarse4 resolution model grids were developed by multiplying the "i-direction" and "j-direction" of the medium-resolution model grid by a factor of 2, 3, and 4, respectively. The simulations were performed for a 24-month period, commencing on January 1, 2017, and ending on December 31, 2018, with January 2017 to June 30, 2017, designated as the warm-up period. The temporal resolution for measured data and model output is 1 hour.

5.2 Summary of results and discussion

The time series plots for water surface elevation (WSE) measurements at three stations (MRMS4, S123_T, and S20GT) were analyzed, comparing observed WSE with model predictions at different resolutions (Fine, Medium, Coarse2, Coarse3, and Coarse4). The analysis of time series plots for water surface elevation (WSE) simulations across the measurement stations and resolutions provides valuable insights into the hydrodynamic modeling process and the impact of grid resolution. The assessment of WSE simulation at three measurement stations consistently showed performance trends across models. The accuracy of model simulations exhibited a gradual

reduction, ranging from -0.1 cm to 1.7 cm, with an increasing trend as resolution decreases. Despite minor variations, there is a general agreement between the different resolutions. Also, the detailed analysis of the Hurricane Irma event highlights model performance variations during this period, emphasizing the need for nuanced calibration to capture event-specific dynamics. These findings underscore the need for careful consideration of resolution effects in hydrodynamic modeling, acknowledging that while resolutions may exhibit subtle differences, they might not significantly impact the overall simulation trends. Modelers should exercise caution when refining models to enhance their predictive capabilities, especially in extreme events, and account for site-specific factors influencing simulation accuracy. The study showed that the resolutions performed similarly in simulating water surface elevation.

Also, the performance of model resolution in simulating salinity distribution across different divisions of the Bay was examined. The models consistently exhibited better simulation of salinity at stations within the Open and South Bay sections (BISC36B, BISC70B, BISCA2, and BISCA4) compared to Nearshore locations (BISCC4 and BISCD4), where they struggled to replicate low salinity levels accurately.

This study underscored the importance of strategic boundary condition measurements for accurate modeling. First, it emphasized the necessity for salinity measurements at the Atlantic Ocean open boundary. The study showed that increasing grid resolution might not necessarily enhance model performance until properly located salinity boundary condition data are obtained. Second, the absence of observed data for the North Bay was identified, highlighting the imperative need to establish measurement stations in this complex region to improve the accuracy of model assessments. Third, the study also highlighted the need for an additional water surface elevation measurement station in the southern portion near the open boundary. These findings call for further

research and management considerations to address these key factors and contribute to model selection and performance evaluation in Biscayne Bay.

5.3 Proposed future work

Hence, we recommend, for future work, the establishment of salinity measurement stations at the tidal open mouths of the Bay or the use of HYbrid Coordinate Ocean Model (HYCOM) salinity data for the tidal BCs. Also, it is essential to install salinity measurement stations in the North Bay. This initiative is crucial for conducting studies that can yield improved results and management recommendations, particularly given the intricate geometry and potential complexities in dynamics.

References

Ahmad, S., & Simonovic, S. P. (1999). Comparison of one-dimensional and two-dimensional hydrodynamic modeling approaches for Red River Basin.

Alarcon, V. J., Linhoss, A. C., Kelble, C. R., Mickle, P. F., Sanchez-Banda, G. F., Fine, A., & Montes, E. (2022). Spatial Distribution of Salinity Under Climate Change: Implications for Restoration of Coastal Biscayne Bay, Florida, USA. SSRN Electronic Journal. https://doi.org/10.2139/ssrn.4234620

Altenau, E. H., Pavelsky, T. M., Bates, P. D., & Neal, J. C. (2017). The effects of spatial resolution and dimensionality on modeling regional-scale hydraulics in a multichannel river. *Water Resources Research*, *53*(2), 1683-1701.

Al-Zubaidi, H. A. (2016). 3D Hydrodynamic Model Development and Verification.

Andrejev, O., Soomere, T., Sokolov, A., & Myrberg, K. (2011). The role of the spatial resolution of a three-dimensional hydrodynamic model for marine transport risk assessment. *Oceanologia*, *53*, 309-334.

Beletsky, D., & Schwab, D. J. (2001). Modeling circulation and thermal structure in Lake Michigan: Annual cycle and interannual variability. Journal of Geophysical Research: Oceans, 106(C9), 19745-19771.

Blumberg, A. F., & Nicholas Kim, B. (2000). Flow balances in St. Andrew Bay revealed through hydrodynamic simulations. Estuaries, 23(1), 21–33.

Blumberg, A. F., & Mellor, G. L. (1987). A description of a three-dimensional coastal ocean circulation model. *Three-dimensional coastal ocean models*, *4*, 1-16.

Burchard, H., Bolding, K., & Villarreal, M. (1999). GOTM, a general ocean turbulence model: Theory, implementation and test cases. *European Commission*. Report EUR 18745.

Bracco, A., Choi, J., Kurian, J., & Chang, P. (2018). Vertical and horizontal resolution dependency in the model representation of tracer dispersion along the continental slope in the northern Gulf of Mexico. *Ocean Modelling*, *122*, 13-25.

Bracco, A., Joshi, K., Luo, H., & McWilliams, J. C. (2015). Submesoscale circulation in the Northern Gulf of Mexico: Deep phenomena and dispersion over the continental slope. *arXiv preprint arXiv:1602.04209*.

Casulli, V., & Cheng, R. T. (1992). Semi-implicit finite difference methods for three-dimensional shallow water flow. International Journal for numerical methods in fluids, 15(6), 629-648.

Casulli, V., & Walters, R. A. (2000). An unstructured grid, three-dimensional model based on the shallow water equations. International journal for numerical methods in fluids, 32(3), 331-348.

Cedillo, P. E. (2015). *Hydrodynamic Modeling of the Green Bay of Lake Michigan Using the Environmental Fluid Dynamics Code.* (Master of Science M.S. thesis). University of Wisconsin-Milwaukee, Milwaukee. Retrieved from https://dc.uwm.edu/etd/1042

Chen, G., Fang, X., & Devkota, J. (2016). Understanding flow dynamics and density currents in a river-reservoir system under upstream reservoir releases. *Hydrological Sciences Journal*, *61*(13), 2411–2426. https://doi.org/10.1080/02626667.2015.1112902

Chen, C., H. Liu, & R. C. Beardsley (2003). An unstructured, finite volume, three-dimensional, primitive equation ocean model: Application to coastal ocean and estuaries, J. Atmos. Oceanic Technol., pp. 20, 159 – 186.

Colberg, F., Brassington, G. B., Sandery, P., Sakov, P., & Aijaz, S. (2020). High and medium resolution ocean models for the Great Barrier Reef. *Ocean Modelling*, *145*, 101507.

Craig, P. M., Chung, D., Lam, N., Son, P., & Tinh, N. (2014, October). Sigma-zed: A computationally efficient approach to reduce the horizontal gradient error in the EFDC's vertical sigma grid. In Proceedings of the 11th International Conference on Hydrodynamics (ICHD, Singapore.

Cunanan, A. M., & Salvacion, J. W. (2016). Hydrodynamic modeling of laguna lake using environmental fluid dynamics code. Int'l Journal of Research in Chemical, Metallurgical and Civil Engg.(IJRCMCE), 3(1).

DAAC (2020). HPC Data Analysis and Assessment Center: Types of Grids. Retrieved July 23, 2023, from https://daac.hpc.mil/gettingStarted/Types_of_Grids.html

Devkota, J., & Fang, X. (2014). Age of Water and Salt Exchange in the Perdido and Wolf Bay System. *World Environmental and Water Resources Congress 2014*, 1292–1301. https://doi.org/10.1061/9780784413548.130

Devkota, J., & Fang, X. (2015). Numerical simulation of flow dynamics in a tidal river under various upstream hydrologic conditions. *Hydrological Sciences Journal*, *60*(10), 1666–1689. https://doi.org/10.1080/02626667.2014.947989

FLOW-3D (2023). Grid Systems. Retrieved October 16, 2023, from https://www.flow3d.com/resources/cfd-101/general-cfd/grid-systems/

Galperin, B., Kantha, L. H., Hassid, S., & Rosati, A. (1988). A quasi-equilibrium turbulent energy model for geophysical flows. Journal of the Atmospheric Sciences, 45(1).

Gupta, H. V., Kling, H., Yilmaz, K. K., & Martinez, G. F. (2009). Decomposition of the mean squared error and NSE performance criteria: Implications for improving hydrological modelling. Journal of hydrology, 377(1-2), 80-91.

Hagen, E. (2014). Hydrodynamic river modelling with D-Flow Flexible Mesh: case study of the side channel at Afferden and Deest (Master's thesis, University of Twente).

Hamrick, J. M. (1996). User's manual for the environmental fluid dynamics computer code.

Hamrick, J. M., (1992). A Three-Dimensional Environmental Fluid Dynamics Computer Code: Theoretical and Computational Aspects. The College of William and Mary, Virginia Institute of Marine Science. Special Report 317, 63 pp.

Hamrick, J. M., & Mills, W. B. (2000). Analysis of water temperatures in Conowingo Pond as influenced by the Peach Bottom atomic power plant thermal discharge. Environmental Science & Policy, 3, 197-209.

Hamrick, J. M., & Wu, T. S. (1997). Computational design and optimization of the EFDC/HEM3D surface water hydrodynamic and eutrophication models. In Next generation environmental models and computational methods (pp. 143-161). Society for Industrial and Applied Mathematics, Philadelphia, PA.

Hashim, N. B. (2001). Watershed, hydrodynamic, and water quality models for total maximum daily load, St. Louis Bay watershed, Mississippi. Mississippi State University.

Haza, A. C., Poje, A. C., Ozgökmen, T. M., & Martin, P. TM Özgökmen, A. Griffa, ZD Garraffo, and L. Piterbarg, 2012: Parameterization of particle transport at submesoscales in the Gulf Stream region using Lagrangian subgridscale models. *Ocean Modell, 42*, 31-49.

Hodges, B., & Dallimore, C. (2010). Estuary, Lake and Coastal Ocean Model: ELCOM v2. 2 Science Manual, Contract Research Group, Centre for Water Research, University of Western Australia, Western Australia.

Horritt, M.S., Bates, P.D., 2001. Effects of spatial resolution on a raster based model of flood flow. J. Hydrol. 253 (1–4), 239–249.

Hua, R., & Zhang, Y. (2017). Assessment of Water Quality Improvements Using the Hydrodynamic Simulation Approach in Regulated Cascade Reservoirs: A Case Study of Drinking Water Sources of Shenzhen, China. *Water, 9*(11), 825. https://doi.org/10.3390/w9110825

Jarihani, A. A., Callow, J. N., McVicar, T. R., Van Niel, T. G., & Larsen, J. R. (2015). Satellite-derived Digital Elevation Model (DEM) selection, preparation and correction for hydrodynamic modelling in large, low-gradient and data-sparse catchments. Journal of Hydrology, 524, 489-506.

Jeong, S., Yeon, K., Hur, Y., & Oh, K. (2010). Salinity intrusion characteristics analysis using EFDC model in the downstream of Geum River. *Journal of Environmental Sciences, 22*(6), 934–939. https://doi.org/10.1016/S1001-0742(09)60201-1

Kate (2006). Ocean Modeling Discussion: Curvilinear Coordinates. Retrieved July 23, 2023, from https://www.myroms.org/forum/viewtopic.php?t=295

Kim, B., Sanders, B. F., Schubert, J. E., & Famiglietti, J. S. (2014). Mesh type tradeoffs in 2D hydrodynamic modeling of flooding with a Godunov-based flow solver. Advances in Water Resources, 68, 42-61.

Knoben, W. J., Freer, J. E., & Woods, R. A. (2019). Inherent benchmark or not? Comparing Nash–Sutcliffe and Kling–Gupta efficiency scores. Hydrology and Earth System Sciences, 23(10), 4323-4331.

Liu, X., & Garcia, M. H. (2008). Numerical Simulation of Density Current in Chicago River Using Environmental Fluid Dynamics Code (EFDC). *World Environmental and Water Resources Congress 2008*, 1–6. https://doi.org/10.1061/40976(316)229

Liu, Z., Hashim, N. B., Kingery, W. L., Huddleston, D. H., & Xia, M. (2008). Hydrodynamic Modeling of St. Louis Bay Estuary and Watershed Using EFDC and HSPF. *Journal of Coastal Research*, *10052*, 107–116. https://doi.org/10.2112/1551-5036-52.sp1.107

LLC, D. (2020). EFDC+ theory, version 10.2.

Luettich, R. A., Westerink, J. J., & Scheffner, N. W. (1992). ADCIRC: an advanced three-dimensional circulation model for shelves, coasts, and estuaries. Report 1, Theory and methodology of ADCIRC-2DD1 and ADCIRC-3DL.

Marvin, J., & Wilson, A. T. (2016). One dimensional, two dimensional and three dimensional hydrodynamic modeling of a Dyked Coastal River in the bay of Fundy. Journal of Water Management Modeling.

Mellor, G. L., & Yamada, T. (1982). Development of a turbulence closure model for geophysical fluid problems. Reviews of Geophysics, 20(4), 851-875.

Moriasi, D.N., Arnold, J.G., Van Liew, M.W., Bingner, R.L., Harmel, R.D., Veith, T.L. (2007). Model Evaluation Guidelines for Systematic Quantification of Accuracy in Watershed Simulations. Trans. ASABE 2007, 50, 885–900, https://doi.org/10.13031/2013.23153

NCEI (National Centers for Environmental Information) (2018). NOAA NOS Estuarine Bathymetry - Biscayne Bay (S200). National Centers for Environmental Information, NOAA. doi:10.7289/V5GM85N8. Accessed on October 27, 2023.

Panda, R. K., Pramanik, N., & Bala, B. (2010). Simulation of river stage using artificial neural network and MIKE 11 hydrodynamic model. Computers & Geosciences, 36(6), 735-745.

Putman, N. F., & He, R. (2013). Tracking the long-distance dispersal of marine organisms: sensitivity to ocean model resolution. *Journal of the Royal Society Interface*, *10*(81), 20120979.

Rantakokko, J. (2000). Partitioning strategies for structured multiblock grids. *Parallel Computing*, *26*(12), 1661-1680.

Roy, S. (2020). Three-dimensional hydrodynamic model set-up: a case study of middle Tennessee River.

Saint-Amand, A., Lambrechts, J., Thomas, C. J., & Hanert, E. (2023). How fine is fine enough? Effect of mesh resolution on hydrodynamic simulations in coral reef environments.

SFWMD (South Florida Water Management District) (2022). DBHYDRO Database. Retrieved from https://apps.sfwmd.gov/WAB/EnvironmentalMonitoring/index.html

NOAA (National Oceanic and Atmospheric Administration) (2022). Water Levels - NOAA Tides & Currents. Retrieved July 22, 2023, from https://tidesandcurrents.noaa.gov/waterlevels.html?id=8723214

Sidoryakina, V. v. (2021). 3D Cartesian vertically boundary-adaptive grids construction for coastal hydrophysics problems. *IOP Conference Series: Materials Science and Engineering*, *1029*, 012116. https://doi.org/10.1088/1757-899X/1029/1/012116

Sidoryakina, V. v., & Sukhinov, A. I. (2017). Well-posedness analysis and numerical implementation of a linearized two-dimensional bottom sediment transport problem. *Computational Mathematics and Mathematical Physics*, *57*(6), 978–994. https://doi.org/10.1134/S0965542517060124

Sukhinov, A. I., Chistyakov, A. E., Protsenko, E. A., Sidoryakina, V. v., & Protsenko, S. v. (2019). A method for taking into account the occupancy of cells for solving problems of hydrodynamics with a complex geometry of the computational domain. *Mathematical Modeling*, *31*(8), 79–100. https://doi.org/10.1134/S0234087919080057

Sukhinov, A. I., Chistyakov, A. E., Protsenko, E. A., Sidoryakina, V. v., & Protsenko, S. v. (2020). Accounting Method of Filling Cells for the Solution of Hydrodynamics Problems with a Complex Geometry of the Computational Domain. *Mathematical Models and Computer Simulations*, *12*(2), 232–245. https://doi.org/10.1134/S2070048220020155

Sukhinov, A. I., Sidoryakina, V. v., & Sukhinov, A. A. (2017). Sufficient conditions for convergence of positive solutions to linearized two-dimensional sediment transport problem. *Vestnik of Don State Technical University*, *17*(1), 5–17. https://doi.org/10.23947/1992-5980-2017-17-1-5-17

UC Davis Math (2012). Derivation of the Navier–Stokes equations. Retrieved January 7, 2024, from https://www.math.ucdavis.edu/~temple/MAT22C/NavierStodesWiki.pdf

Vreugdenhil, C. B. (1994). Numerical methods for shallow-water flow (Vol. 13). Springer Science & Business Media.

Wang, Y., Jiang, Y., Liao, W., Gao, P., Huang, X., Wang, H., Song, X. & Lei, X. (2014). 3-D hydro-environmental simulation of Miyun reservoir, Beijin. Journal of Hydro-environment Research, 8(4), 383-395.

Xia, M., Craig, P. M., Wallen, C. M., Stoddard, A., Mandrup-Poulsen, J., Peng, M., Schaeffer, B., & Liu, Z. (2011). Numerical Simulation of Salinity and Dissolved Oxygen at Perdido Bay and Adjacent Coastal Ocean. *Journal of Coastal Research*, *27*(1), 73. https://doi.org/10.2112/JCOASTRES-D-09-00044.1

Yin, Z., & Seo, D. (2016). Analysis of optimum grid determination of water quality model with 3-D hydrodynamic model using environmental fluid dynamics code (EFDC).

Environmental Engineering Research, *21*(2), 171–179. https://doi.org/10.4491/eer.2015.137

Zhong, Y., & Bracco, A. (2013). Submesoscale impacts on horizontal and vertical transport in the Gulf of Mexico. Journal of Geophysical Research: Oceans, 118(10), 5651-5668.